

# Performance optimization of Lead-free $\text{MASnBr}_3$ based perovskite solar cells by SCAPS-1D device simulation

Shammas Mushtaq<sup>a</sup>, Sofia Tahir<sup>a,b</sup>, Arslan Ashfaq<sup>a\*</sup>, Ruy Sebastian Bonilla<sup>b</sup>, Muhammad Haneef<sup>a</sup>, Rabia Saeed<sup>a</sup>, Waqas Ahmad<sup>a</sup>, Nasir Amin<sup>a</sup>

<sup>a</sup>Department of Physics, Government College University, Faisalabad, 3800, Pakistan

<sup>b</sup>Department of Materials, University of Oxford, OX1-3PH, United Kingdom

[\\*arslan.ashfaq201@gmail.com](mailto:arslan.ashfaq201@gmail.com)

Perovskites are at the forefront of research into potential alternatives for bulky and costly silicon-based solar cells. In recent years, lead-based organic and inorganic perovskite solar cells have broken efficiency records. However, these have stability issues and may pose health risks in the long-term. Hence, there has been ideally inorganic perovskite solar cells and parallel search for lead-free to match and eventually surpass the achievements of lead perovskite analogues. This study reports a modelling-guided device optimization process to design highly efficient lead-free n-i-p methyl ammonium tin bromide ( $\text{MASnBr}_3$ ) perovskite solar cells. We have studied the effect of the various hole and electron transport layers on the performance of  $\text{MASnBr}_3$  devices. The influence of different parameters, such as doping concentration of optimized HTLs/ETLs, the thickness of the perovskite layer,  $N_A/N_D$  of the absorption layer, and the defect density, is thoroughly investigated using numerical simulations. An optimized device FTO/ $\text{SnO}_2$ / $\text{MASnBr}_3$ / $\text{NiO}$ /Au is proposed here with an open circuit voltage of 1.1214 V, a short circuit current density of 34.8654  $\text{mA}/\text{cm}^2$ , fill factors of 88.30 %, a theoretical power conversion efficiencies of 34.52 %, and quantum efficiencies of 98 %. This work reveals the potential of the  $\text{MASnBr}_3$  material as a perovskite for toxicity-free renewable energy.

**Keywords:** Perovskite solar cell, lead-free,  $\text{MASnBr}_3$ , SCAPS-ID, HTLs, ETLs

## 1. Introduction

1 The perovskite structure solar cell continues to attract the interest of the solar energy world due  
2 to their highly high packing conversion efficiency and associated best electrical and optical  
3 properties. Perovskite solar cells have provided additional advantages such as being cost-  
4 effective, manufacturing at room temperatures, a direct energy band gap, reduced exciton  
5 binding energy, and improved light absorption. The amount of incident sunlight converts into  
6 electrical energy using the photovoltaic effect. The commercially used solar cells have high open  
7 circuit voltage ( $V_{oc}$ ), short circuit current density ( $J_{sc}$ ), fill factor (FF) and packing conversion  
8 efficiency (PCE). The hole transport material layer, an electron transport material layer, and  
9 absorber layer are required in a perovskite solar cell for effective energy conversion. Because  
10 experimental manufacturing of the various levels of a multi-layered perovskite solar cell is costly  
11 and time-consuming, simulation studies and computational modelling are vital for identifying  
12 acceptable materials for different layers of perovskite solar cells (Lakhdar and Hima, 2020).

13 The structure of perovskite solar cell (PSC) has used the ABX general formula, where A cation  
14 is the formamidinium ( $CHNH_3^+ = NH$ ) ion or an organic like methyl ammonium ( $CH_3NH_3^+$ ) ion,  
15 B is an inorganic cation such as  $Sn^{2+}$  or  $Pb^{2+}$ , and X is the halogen ion  $Cl^-$ ,  $Br^-$ ,  $I^-$ . We have used  
16 the halogen ion ( $Br^-$ ) in the current study of perovskite layer. The most common absorber  
17 material for PSC is methyl ammonium lead iodide ( $MAPbI_3$ ) (Eperon et al., 2014; Kazim et al.,  
18 2014). However, the hazardous nature of lead (Pb) prohibits its widespread usage in some  
19 commercial applications. Alternatively, the poisonous Pb ion in  $MAPbI_3$  is substituted with  
20 Germanium (Ge) or tin (Sn). The resulting perovskite structures are considered helpful as  
21 absorber perovskite structure materials for solar cells with high packing conversion efficiency.  
22 Recently, perovskite structures have been proposed as possible absorber layers in solar cells  
23 without the need for lead (Al-Douri et al., 2015; Ashfaq et al., 2019; Devi and Mehra, 2019). The

effects of interface defect states and amphoteric defect states on the photovoltaic (PV) properties of  $\text{MASnBr}_3$  perovskite solar cell were investigated using numerical modelling (Samiul Islam et al., 2021). The octahedral factor and the Goldschmidt tolerance factor have theoretically supported the  $\text{MASnBr}_3$  perovskite structure (Kour et al., 2019; McMeekin et al., 2016). Therefore, it can be claimed that the suggested perovskite structure ( $\text{MASnBr}_3$ ) can be an excellent contender for lead free highly efficient and most stable PSC.

The maximum efficiency of the perovskite layer is achieved by using an ETM to extract the generated photoelectrons by the absorber material and an HTM to improve the hole extraction. The nature and kind of these layers significantly impact the stability and device performance. The maximum PCE is attained when  $\text{TiO}_2$  is utilized as the ETM in PSCs (Lv et al., 2020). However, the rutile phase of  $\text{TiO}_2$  is mainly used in solar cell applications, which are obtained at a high post-annealing temperature. The  $\text{TiO}_2$  material application as an ETL in PSCs is limited due to the high-temperature processing required (Kolaczowski and Thornton, 2004; Yang et al., 2017). In the same way, mostly used carbon-based HTMs such as PEDOT: PSS and Spiro-OMeTAD are unsuitable for solar cells due to stability and cost limits. As a result, researchers have also carefully chosen different ETM and HTM transport layers to maximize device performance. (Jayan and Sebastian, 2021; Pindolia et al., 2022). When titanium dioxide is used as the electron transport material layer and  $\text{CuSCN}$  is employed as the hole transport material layer, a perovskite structure solar cell with  $\text{MASnI}_3$  as the absorber material layer simulated the maximum PCE of 28.32 % (Devi and Mehra, 2019). When zinc oxide is utilized as electron transport material layer and  $\text{CuO}_2$ , PEDOT: PSS and SpiroMeOTAD as HTM, the efficiency of 25.36 %, 24.50 % and 24.17 %, respectively, was numerically simulated (Slami et al., 2020). Another modelling work for  $\text{MASnI}_3$  perovskite layer solar cells using  $\text{CuI}$  as HTL and  $\text{ZnO}$  as

ETL finds an efficiency of 24.82 % (Mandadapu et al., 2017). The stability, cost effective, processing temperature, defect, thickness and doping density are directly influenced on the best HTM/ETM. The different groups are also working on the various perovskite structures using different HTM/ETM and doping ratios to enhance the solar cell performance.

In the current study, we have studied the  $\text{MASnBr}_3$  perovskite solar cell by different HTLs ( $\text{Cu}_2\text{O}$ ,  $\text{CuSbS}_2$ ,  $\text{CuI}$ ,  $\text{NiO}$  and Spiro-OMeTAD) and ETLs ( $\text{SnO}_2$ ,  $\text{TiO}_2$ ,  $\text{WS}_2$ ,  $\text{CdS}$ ,  $\text{ZnO}$ ). We have optimized the thickness and doping concentration of all HTLs and ETLs as well as the thickness of the absorber layer, acceptor and donor doping charge concentration of the absorption layer, defect density of perovskite layer, interface defect density of the HTL/perovskite layer, and perovskite layer/ETL, back contact work function, series and shunt resistance. The optimized structure performance at a different temperature, a FF was achieved 88.30 %, and PCE is 34.52 %.

## **2. Simulation structure**

Solar Cell Capacitance Simulator-one Dimension (SCAPS-1D) version 3.3.10 was used in this work because of its benefits, including control and ease of use, modelling of both bright and dark environments, and the ability to create a seven different layer heterostructure system using SCAPS (Anwar et al., 2017; Khadka et al., 2018). SCAPS-1D was developed by Marc Burgelman and his colleagues at the University of Gent's, Belgium.

SCAPS-1D can calculate many values such as energy band, short circuit current density ( $J_{sc}$ ), quantum efficiency (QE), open circuit voltage ( $V_{oc}$ ), packing conversion efficiency (PCE), fill factor (FF) and current-voltage (JV) properties to assess the performance of solar cells by solving

1 the three equations such as poisson equation, the continuity equation for electron and continuity  
2 equation for the hole.

3 Poisson equation:  $-\frac{\partial}{\partial x}\left(-\varepsilon(x)\frac{\partial V}{\partial x}\right) = q[p(x) - n(x) + N_D^+(x) - N_A^-(x) + p_t(x) - n_t(x)]$  (i)

4 Continuity equation for the hole:  $\frac{\partial p}{\partial t} = \frac{1}{q} \frac{\partial J_p}{\partial x} + G_p - R_p$  (ii)

5 Continuity equation for electron:  $\frac{\partial n}{\partial t} = \frac{1}{q} \frac{\partial J_n}{\partial x} + G_n - R_n$  (iii)

6 Where  $q$  is the charge,  $\varepsilon$  is the dielectric permittivity,  $V$  is the potential,  $p(x)$  is the free holes  
7 concentration,  $n(x)$  is the free electrons concentration,  $N_D^+(x)$  is the ionized donor concentration,  
8  $N_A^-(x)$  is the ionized acceptor concentration,  $p_t(x)$  is the hole trap density,  $n_t(x)$  is the trap density  
9 of electron,  $J_n$  is the current density of electron,  $J_p$  is the current density of hole,  $G_n$  is the  
10 electrons generation rate,  $G_p$  is the holes generation rate,  $R_n$  is the recombination rate of an  
11 electron,  $R_p$  is the recombination rate of the hole.

12 Figure 1 (a) illustrates an n-i-p planner structure of PSC, which contains Au as back contact,  
13 CuSbS<sub>2</sub> as the hole transport layer, CH<sub>3</sub>-NH<sub>3</sub>SnBr<sub>3</sub> as perovskite layer, TiO<sub>2</sub> as the electron  
14 transport layer and FTO as front contact glass. The initial simulation is used of this PSC-  
15 described structure. The initial structure input parameters are shown in Table 1, compiled from  
16 theories and earlier works. Here  $d$  is the thickness,  $E_g$  is the bandgap,  $\chi$  is the electron affinity,  $\varepsilon_r$   
17 is the dielectric permittivity,  $N_C$  is the conduction band effective density of state,  $N_V$  is the  
18 valence band effective density of states,  $\mu_p$  is the mobility of holes,  $\mu_e$  is the mobility of  
19 electrons,  $N_A$  is the acceptor concentration,  $N_D$  is the donor concentration, and  $N_T$  is the defect  
20 concentration (Hima and Lakhdar, 2020; Ju et al., 2018; Samiul Islam et al., 2021).

1 The temperature is taken to be 300 K for a constant illumination  $1000 \text{ Wm}^{-2}$  at AM 1.5G. The  
2 thermal velocity of electrons and holes is kept as  $10^7 \text{ cm/s}$ . The  $\text{TiO}_2/\text{MASnBr}_3$  and  
3  $\text{MASnBr}_3/\text{CuSbS}_2$  interface layers are used to perfect a more accurate perovskite solar cell. It is  
4 taken that both interfaces have neutral defect densities of  $10^{14} \text{ cm}^{-2}$  with distinctive energy of 0.1  
5 eV. The back contact work function of Au is taken to be 5.1 eV. We have taken acceptor and  
6 donor doping concentration ( $N_A$  &  $N_D$ ) of  $\text{MASnBr}_3$  as  $10^{+13}$ . We will modify  $N_A$  and  $N_D$  in the  
7 study to determine their optimal levels. The hole transport layer ( $\text{CuSbS}_2$ ) was optimized in the  
8 literature with maximum open-circuit voltage (Hima and Lakhdar, 2020). The initial calculated  
9 parameters are follows such as  $V_{oc} = 1.0038 \text{ V}$ ,  $J_{sc} = 35.2528 \text{ mA/cm}^2$ ,  $\text{FF} = 67.71 \%$  and  $\text{PCE} =$   
10  $23.97 \%$ .

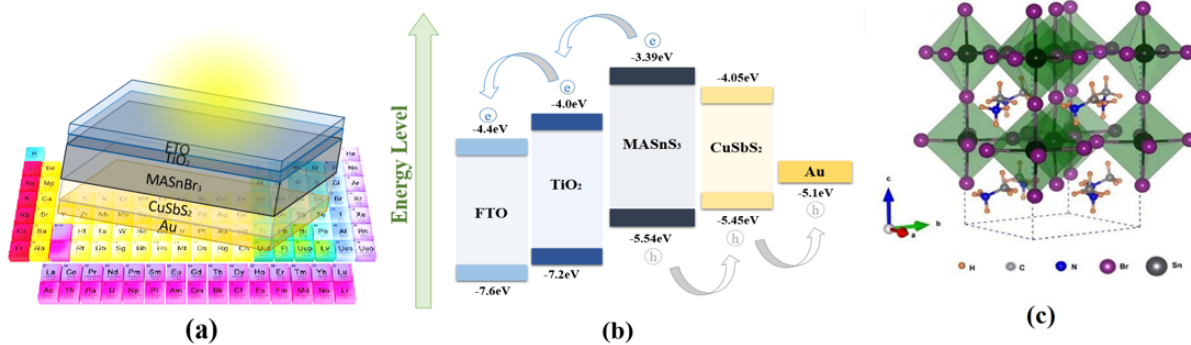


Figure 1 (a) Configuration of the Initial Device (b) Initially configured energy bands (c)  
MASnBr<sub>3</sub> structure

Table 1 shows the SCAPS-1D input initial device parameters configuration

Properties	$\text{CuSbS}_2$	$\text{MASnBr}_3$	$\text{TiO}_2$	FTO
$d \text{ (}\mu\text{m)}$	0.40	0.50	0.05	0.40
$E_g \text{ (eV)}$	1.58	1.30	3.26	3.50
$\chi \text{ (eV)}$	4.20	4.17	4.2	4.00

$\epsilon_r$ (eV)	8.2	10.00	10	9.00
$N_C$ (1/cm <sup>3</sup> )	$2.0 \times 10^{18}$	$2.2 \times 10^{18}$	$2.2 \times 10^{18}$	$2.2 \times 10^{18}$
$N_V$ (1/cm <sup>3</sup> )	$1.0 \times 10^{19}$	$1.8 \times 10^{18}$	$1.8 \times 10^{18}$	$1.8 \times 10^{18}$
$\mu_e$ (cm <sup>2</sup> /Vs)	$4.9 \times 10^1$	$1.6 \times 10^0$	$2.0 \times 10^1$	$2.0 \times 10^1$
$\mu_p$ (cm <sup>2</sup> /Vs)	$4.9 \times 10^1$	$1.6 \times 10^0$	$1.0 \times 10^1$	$1.0 \times 10^1$
$N_D$ (1/cm <sup>3</sup> )	0	$1.0 \times 10^{13}$	$1.0 \times 10^{17}$	$1.0 \times 10^{19}$
$N_A$ (1/cm <sup>3</sup> )	$1.38 \times 10^{18}$	$1.0 \times 10^{13}$	0	0
$N_T$ (1/cm <sup>3</sup> )	$1.0 \times 10^{14}$	$1.0 \times 10^{14}$	$1.0 \times 10^{14}$	$1.0 \times 10^{14}$

### 3. Results and Discussion

#### 3.1 Optimization of HTL

The hole transport material (HTM) effects the device efficiency of PSCs via blocking electrons, reducing the electron-hole recombination rate and facilitating hole migration from the MASnBr<sub>3</sub> (absorber) layer to the Au (back contact layer). The HTM must have an appropriate bandgap, positive charge carrier mobility, optimum thickness, and optimal doping charge concentration (Saikia et al., 2022).

In this part, we simulate the solar device efficiency in the original device configuration FTO/TiO<sub>2</sub>/MASnBr<sub>3</sub>/HTL/Au using several hole transport layers (NiO, Cu<sub>2</sub>O, CuI, CuSbS<sub>2</sub>, and Sprio-OMeTAD). Table 2 shows the various HTLs input parameters (Ahmed et al., 2021; Hima and Lakhdar, 2020; Saikia et al., 2022), and the energy level schematic diagram of different HTLs is illustrated in figure 2. The J-V characteristics for various HTLs are illustrated in figure 3. The efficiency of perovskite solar devices with various HTLs is charted as shown in table 3.

All hole transport layers, including the organic (Sprio-OMeTAD) and inorganic (NiO, Cu<sub>2</sub>O, CuI, CuSbS<sub>2</sub>) shows the maximum higher current density ( $J_{sc}$ ). The hole mobility of all hole

transport layers, including the organic and inorganic, have the same and high. The high charge carrier mobility is the reason for the high current density (Gu et al., 2019). According to figure 2, the valence band offsets for NiO, Cu<sub>2</sub>O, CuI, CuSbS<sub>2</sub>, and Spiro-OMeTAD are -0.34, -0.37, -0.46, -0.09 and -0.61, respectively. When valence band offset is negative, there is no barrier for photogenerated holes to flow toward the hole transport layers; hence  $J_{sc}$  is essentially constant (Ahmed et al., 2021). We determined the  $J_{sc}$  is 35.26 mA/cm<sup>2</sup> for NiO, Cu<sub>2</sub>O, CuI, CuSbS<sub>2</sub>, and Spiro-OMeTAD, respectively. But the positive value of the valence band offset creates a barrier that prevents photogenerated holes from flowing from the absorber to the HTLs. In the current study, valence band offsets of the all layer's are negative, indicating that they are all potential candidates to develop into HTLs. However, a large negative value of VBO leads to a concentration of holes at the interface between the HTL and the absorber layer, resulting in a recombination process at the absorber/HTL. Therefore, a material with moderate negative valence band offset should be considered for improved band alignment, resulting in good performance of the device. Table 3 shows that the nickel oxide gives better FF and PCE. The FF improve from 67.71 % to 81.13 %, and PCE improves from 23.97 % to 29.21%. We choose NiO for further simulations after balancing a significant rise in FF and PCE. The PSC device using NiO as HTL has  $V_{oc} = 1.0209$  V,  $J_{sc} = 35.2526$  mA/cm<sup>2</sup>, FF = 81.13 % and PCE = 29.21 %.

The hole transport layer thickness varies from (100-1000) nm to evaluate the impact of this thickness on the efficiency of perovskite structure solar cells. The difference in device efficiency with HTL thickness is seen in figure 4. The PV parameters of hole transport material layers are nearly identical, with a slight thickness variation. The FF and PCE for CuSbS<sub>2</sub> and Spiro-OMeTAD after 300 nm slightly change to the other hole transport layer. This might be due to CuSbS<sub>2</sub> and Spiro-OMeTAD layers having lower charge motilities and conductivity when



compared with other HTLs. Comparing it to the other HTLs, increasing the thickness of  $\text{CuSbS}_2$  and spiro-OMeTAD will slightly raise the resistance of the layers (Raoui et al., 2019). NiO at 200 nm provides better performance for the device. Hence, NiO (200 nm) is selected as the optimum hole transport layer. NiO (HTL) based devices have the highest efficiency achieved to their increased carrier mobility and an appropriate VBO, which results in a higher FF and PCE.

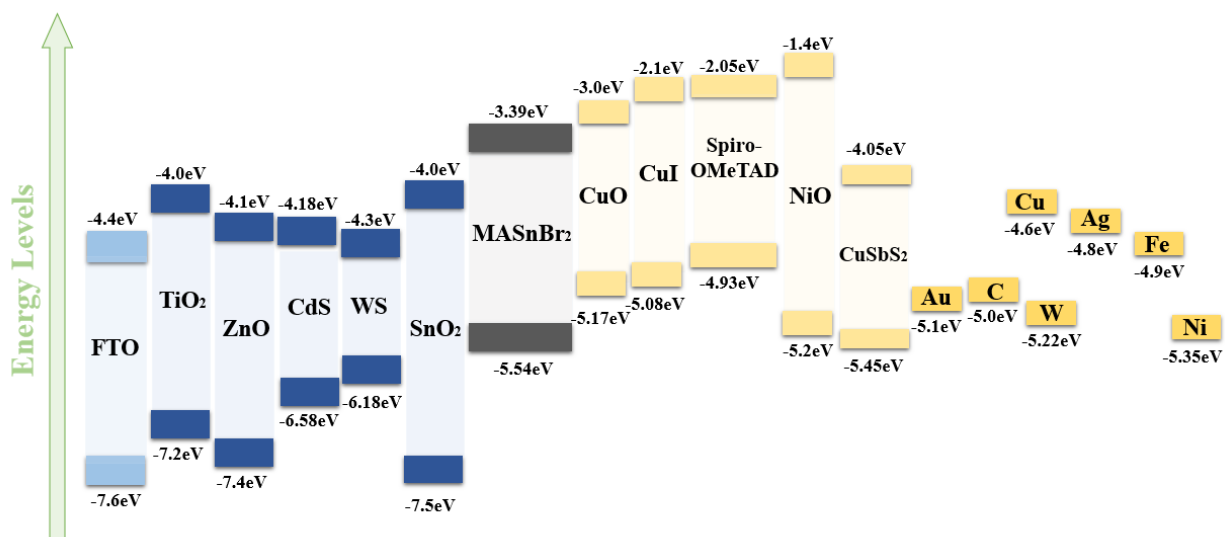


Figure 2 Various HTMs, ETMs,  $\text{MASnBr}_3$ , rear contacts, and front contacts all have different energy bands

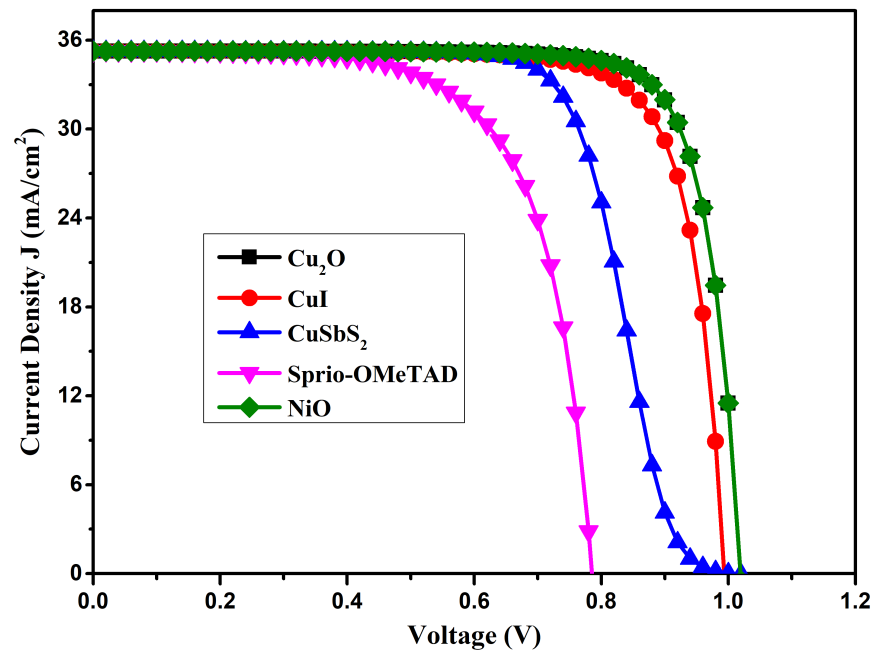


Figure 3 JV curve for different hole transport material

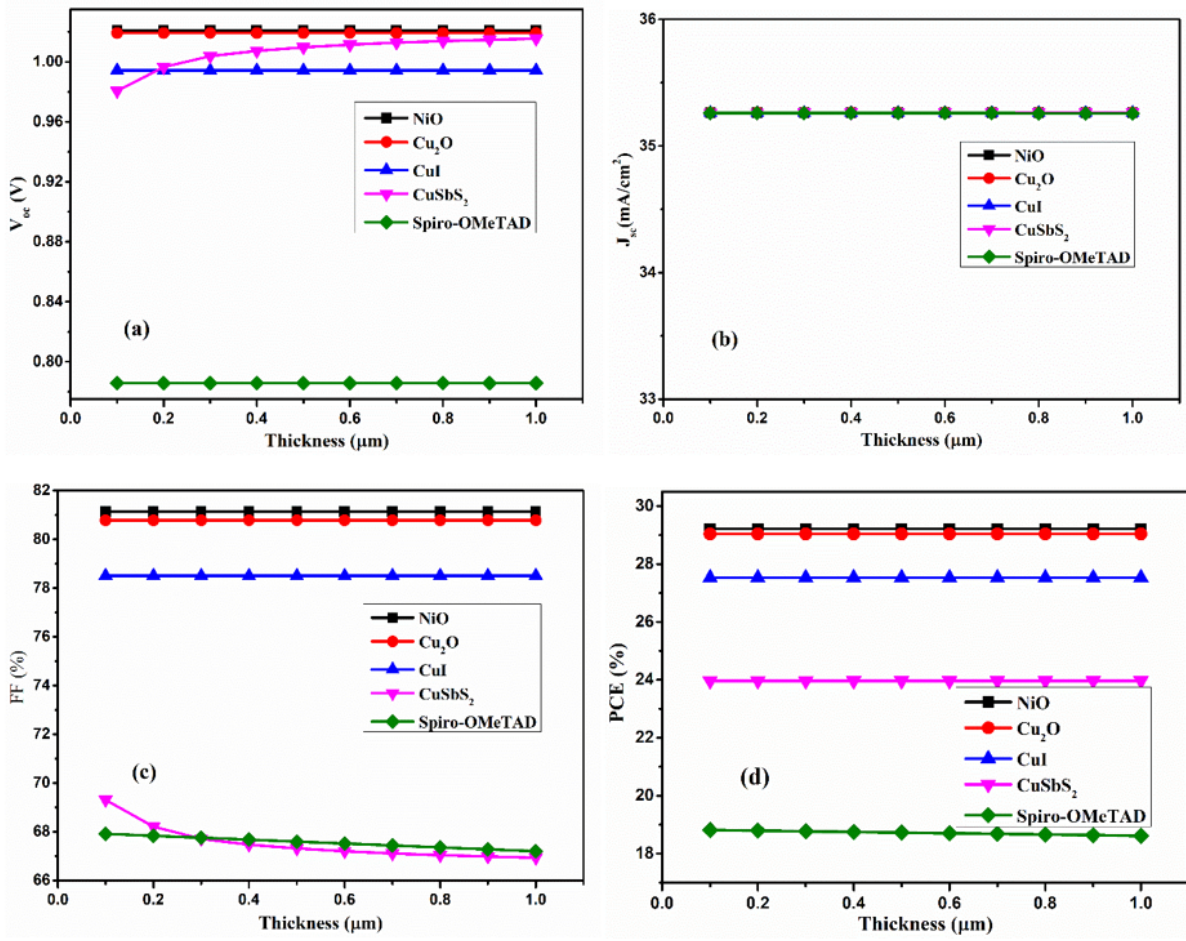


Figure 4 Variation of PSc device performance with hole transport layer thickness

Table 2 SCAPS-1D input settings for various HTLs

Properties	CuSbS <sub>2</sub>	NiO	Cu <sub>2</sub> O	Spiro-OMeTAD	CuI
d (μm)	0.40	0.15	0.20	0.20	0.20
E <sub>g</sub> (eV)	1.58	3.60	2.17	2.88	2.98
χ (eV)	4.20	1.80	3.00	2.05	2.10
ε <sub>r</sub> (eV)	8.2	11.70	7.50	3.00	6.50
N <sub>c</sub> (1/cm <sup>3</sup> )	2.0×10 <sup>18</sup>	2.5×10 <sup>20</sup>	2.0×10 <sup>18</sup>	2.5×10 <sup>20</sup>	2.8×10 <sup>19</sup>
N <sub>v</sub> (1/cm <sup>3</sup> )	1.0×10 <sup>19</sup>	2.5×10 <sup>20</sup>	1.1×10 <sup>19</sup>	2.5×10 <sup>20</sup>	1.1×10 <sup>19</sup>

$\mu_e$ (cm <sup>2</sup> /Vs)	$4.9 \times 10^1$	$2.8 \times 10^0$	$2.0 \times 10^2$	$2.1 \times 10^{-3}$	$1.0 \times 10^2$
$\mu_p$ (cm <sup>2</sup> /Vs)	$4.9 \times 10^1$	$2.8 \times 10^0$	$8.0 \times 10^1$	$2.6 \times 10^{-3}$	$4.39 \times 10^1$
$N_D$ (1/cm <sup>3</sup> )	0	0	0	0	0
$N_A$ (1/cm <sup>3</sup> )	$1.38 \times 10^{18}$	$3.0 \times 10^{18}$	$2.0 \times 10^{19}$	$1.0 \times 10^{18}$	$2.0 \times 10^{19}$
$N_T$ (1/cm <sup>3</sup> )	$1.0 \times 10^{14}$	$1.0 \times 10^{14}$	$1.0 \times 10^{15}$	$1.0 \times 10^{15}$	$1.0 \times 10^{15}$

Table 3 PSC device performance using TiO<sub>2</sub> as the ETL and various HTLs

Device Structure	$V_{oc}$ (V)	$J_{sc}$ (mA/cm <sup>2</sup> )	FF (%)	PCE (%)
FTO/TiO <sub>2</sub> /MASnBr <sub>3</sub> /NiO/Au	1.0209	35.2626	81.13	29.21
FTO/TiO <sub>2</sub> /MASnBr <sub>3</sub> /Cu <sub>2</sub> O/Au	1.0192	35.2640	80.78	29.04
FTO/TiO <sub>2</sub> /MASnBr <sub>3</sub> /CuI/Au	0.9942	35.2624	78.51	27.52
FTO/TiO <sub>2</sub> /MASnBr <sub>3</sub> /CuSbS <sub>2</sub> /Au	1.0038	35.2628	67.71	23.97
FTO/TiO <sub>2</sub> /MASnBr <sub>3</sub> /Spiro-OMeTAD/Au	0.7857	35.2602	67.75	18.79

### 3.2 Optimization of the HTL doping density

The hole transport layers significantly impact the PSC device performance with charge carrier concentration. To investigate the effects of HTL doping density on the PSC device efficiency, we calculate the PSC device efficiency by changing the acceptor doping charge concentration ( $N_A$ ) of the hole transport layer from  $10^{16}$  cm<sup>3</sup> to  $10^{20}$  cm<sup>3</sup>. The fluctuation of each device parameter for the  $N_A$  of the hole transport material layer is shown in figure 5. The FF and PCE of PSC device parameters significantly increase the doping concentration to  $10^{20}$  cm<sup>3</sup>, but the  $V_{oc}$  and  $J_{sc}$  slightly decrease with increasing the doping charge concentration up to  $10^{19}$  cm<sup>3</sup>. The PSC device parameters rapidly rise as HTL doping concentration is raised further. This improvement in the performance of the device is caused by the fact that when doping charge concentration rises, the HTLs internal electric field also rises, increasing the charge transport velocity and

conductivity (Ghosh et al., 2020). However, excessive doping causes the formation of coulomb traps, which reduces the hole's mobility (Saikia et al., 2022). Therefore, for future simulations, we maintain the optimum acceptor doping concentration ( $N_A$ ) of the HTL at  $10^{20} \text{ cm}^{-3}$ . According to the best PSC device efficiency:  $V_{oc} = 1.0219 \text{ V}$ ,  $J_{sc} = 35.2618 \text{ mA/cm}^2$ ,  $FF = 82.25 \%$  and  $PCE = 29.64 \%$ .

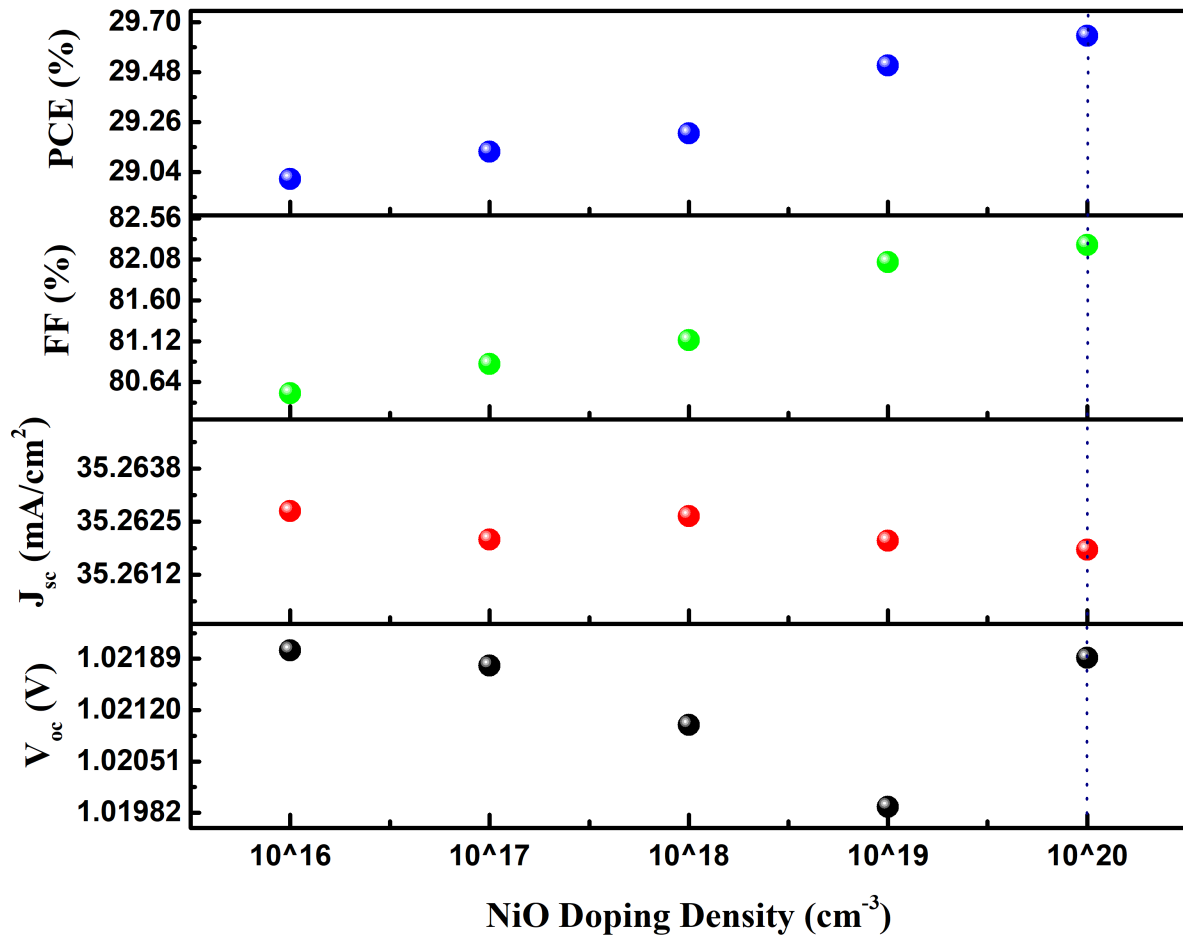


Figure 5 The PSC performance varies depending on the amount of HTL doping

### 3.3 Optimization of ETL

The electron transport layer improves electron transport via decreasing electron-hole recombination and blocking photogenerated holes. The best ETL must have high electron mobility, appropriate doping concentration and thickness, and a proper bandgap.

The perovskite solar cell performance of the device is calculated utilizing several ETLs (CdS, TiO<sub>2</sub>, WS<sub>2</sub>, ZnO, and SnO<sub>2</sub>) with the solar cell structure FTO/ETL/MASnBr<sub>3</sub>/NiO/Au using optimal NiO (HTL) with doping concentration ( $10^{20} \text{ cm}^{-3}$ ). The photogenerated electrons from the perovskite are collected and delivered to the upper contact through ETL. Table 4 displays the input parameters of several electron transport layers (Ahmed et al., 2021; Lakhdar and Hima, 2020; Saikia et al., 2022). Table 5 lists the perovskite solar cell device performance for various ETLs. The JV curve of different electron transport materials is shown in figure 6.

According to Figure 2, the conduction band offsets (CBO) for TiO<sub>2</sub>, SnO<sub>2</sub>, ZnO, CdS, and WS<sub>2</sub> is - 0.61, - 0.61, - 0.71, - 0.79, and - 0.91 eV, respectively. The flow of photogenerated electrons is impeded by materials with positive CBO, whereas those with negative conduction band offset permit the easy flow of photogenerated electrons (Ahmed et al., 2021). Every layer in the current analysis has a negative CBO, suggesting they are all potential candidates to become ETLs. However, a high negative CBO leads electrons to accumulate at the absorber/ETL contact, which results in recombination there. Therefore, a material with a low negative conduction band offset should be considered for improved band alignment, resulting in improved PSC performance of the device. Table 5 demonstrates that of all the ETLs, WS<sub>2</sub> has the weakest performance and has the biggest negative CBO. The smaller bandgap of WS<sub>2</sub> contributes to its subpar performance (Liu et al., 2014). Hence, WS<sub>2</sub> will have the lowest JV due to having the smallest bandgap and the least amount of light absorption. SnO<sub>2</sub> performs best with  $V_{oc} = 1.0242 \text{ V}$ ,  $J_{sc} = 352548 \text{ mA/cm}^2$ ,  $FF = 82.44 \%$ , and  $PCE = 29.77 \%$  due to its low negative conduction band offset.

We change the thickness of the electron transport material from 0.01  $\mu\text{m}$  to 0.1  $\mu\text{m}$  to examine the impact of ETL thickness on the efficiency of perovskite structure solar cells. The perovskite solar cell performance as a function of ETL thickness is depicted in figure 7.  $\text{SnO}_2$ -based PSCs have minimal performance fluctuation with ETL thickness. The ETL's have almost the same  $J_{\text{sc}}$  and PCE values, except for  $\text{CdS}$  and  $\text{WS}_2$ , whose PCE marginally drops up to 100 nm. The FF of every ETLs remains the same as thickness increases.  $V_{\text{oc}}$  of  $\text{WS}_2$  drops significantly with thickness. This drop is caused by the fact that as electron transport layer thickness rises, the layer's series resistance and the likelihood of recombination both rise (Saikia et al., 2022).  $\text{SnO}_2$  provides the best device performance at 10 nm. As a result,  $\text{SnO}_2$  (10 nm) is selected as the ideal ETL.

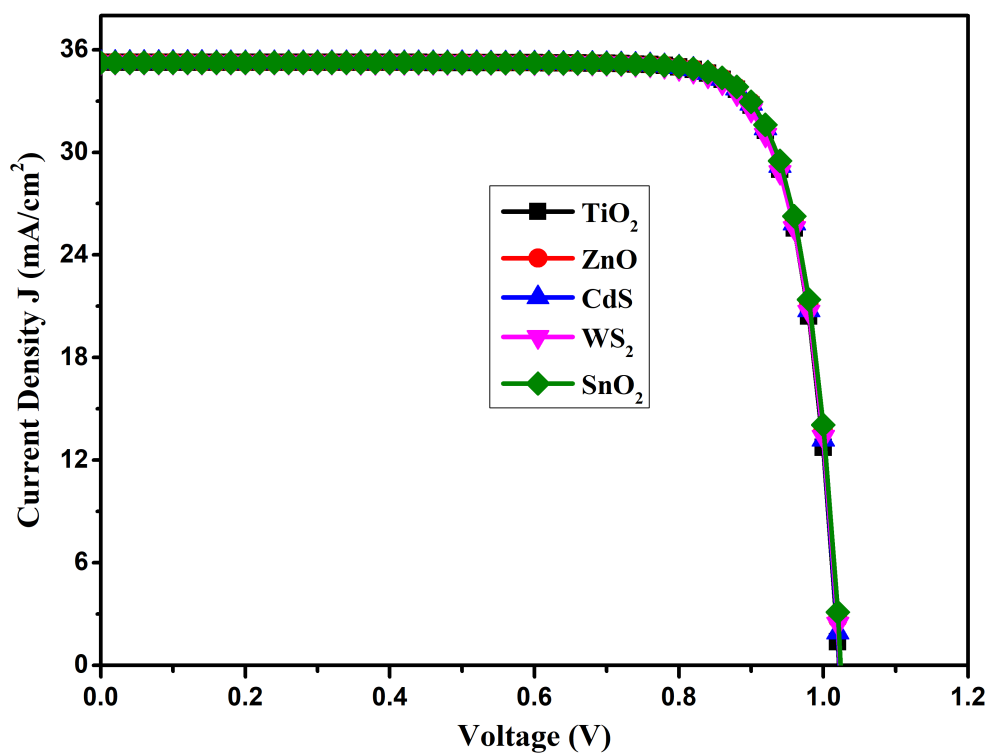


Figure 6 JV curve for different electron transport material

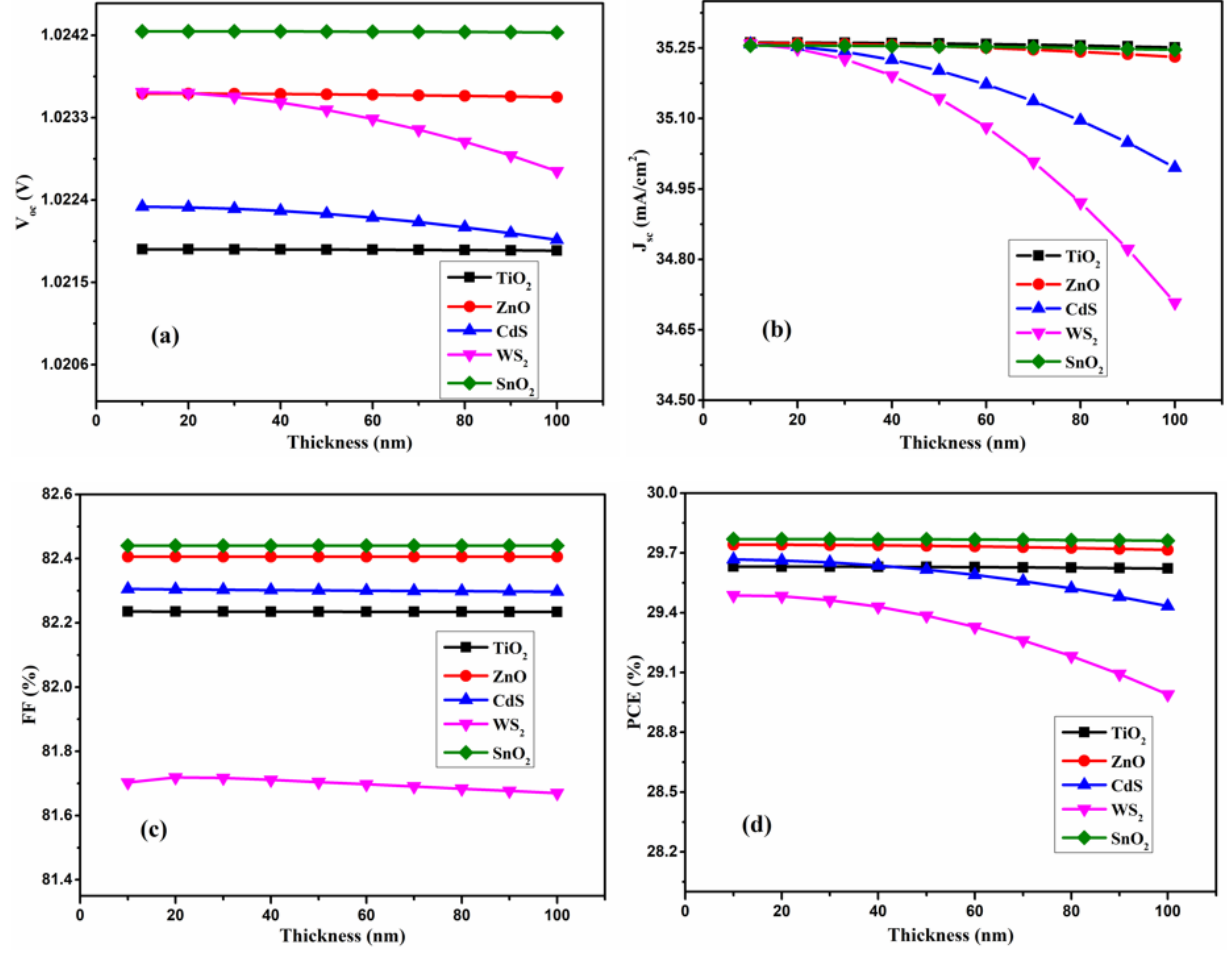


Figure 7 the variation of PSC efficiency with electron transport layer thickness

Table 4 the SCAPS-1D input settings for different ETLs

Properties	TiO <sub>2</sub>	ZnO	CdS	WS <sub>2</sub>	SnO <sub>2</sub>
d (μm)	0.05	0.03	0.03	0.03	0.03
E <sub>g</sub> (eV)	3.26	3.30	2.40	1.87	3.30
χ (eV)	4.2	4.1	4.18	4.30	4.00
ε <sub>r</sub> (eV)	10	9.00	10.00	11.90	9.00
N <sub>C</sub> (1/cm <sup>3</sup> )	2.2×10 <sup>18</sup>	2.2×10 <sup>18</sup>	2.2×10 <sup>18</sup>	1.0×10 <sup>19</sup>	2.2×10 <sup>17</sup>
N <sub>V</sub> (1/cm <sup>3</sup> )	1.8×10 <sup>18</sup>	1.9×10 <sup>19</sup>	1.9×10 <sup>19</sup>	2.4×10 <sup>19</sup>	2.2×10 <sup>16</sup>
μ <sub>e</sub> (cm <sup>2</sup> /Vs)	2.0×10 <sup>1</sup>	1.0×10 <sup>2</sup>	1.0×10 <sup>2</sup>	2.6×10 <sup>2</sup>	2.0×10 <sup>2</sup>



$\mu_p$ (cm <sup>2</sup> /Vs)	$1.0 \times 10^1$	$2.5 \times 10^1$	$4.39 \times 10^1$	$5.1 \times 10^1$	$8.0 \times 10^1$
$N_D$ (1/cm <sup>3</sup> )	$1.0 \times 10^{17}$	$1.0 \times 10^{17}$	$1.0 \times 10^{17}$	$1.0 \times 10^{17}$	$1.0 \times 10^{17}$
$N_A$ (1/cm <sup>3</sup> )	0	0	0	0	0
$N_T$ (1/cm <sup>3</sup> )	$1.0 \times 10^{14}$	$1.0 \times 10^{15}$	$1.0 \times 10^{15}$	$1.0 \times 10^{15}$	$1.0 \times 10^{15}$

Table 5 The PSC performance using NiO (200 nm) as the HTL and various ETLs.

PSC Structure	$V_{oc}$ (V)	$J_{sc}$ (mA/cm <sup>2</sup> )	FF (%)	PCE (%)
FTO/TiO <sub>2</sub> /MASnBr <sub>3</sub> /NiO/Au	1.0218	35.2611	82.23	29.63
FTO/ZnO/MASnBr <sub>3</sub> / NiO /Au	1.0235	35.2586	82.41	29.74
FTO/CdS/MASnBr <sub>3</sub> / NiO /Au	1.0223	35.2420	82.30	29.65
FTO/WS <sub>2</sub> /MASnBr <sub>3</sub> / NiO /Au	1.0235	35.2262	81.72	29.46
FTO/SnO <sub>2</sub> /MASnBr <sub>3</sub> / NiO /Au	1.0242	35.2548	82.44	29.77

### 3.4 Optimization of the ETL doping density

The electron transport material with electron charge carrier concentration significantly impacts on the PSC efficiency. We calculate the PSC efficiency by changing the donor doping charge concentration ( $N_D$ ) of the electron transport layer from  $10^{14}$  cm<sup>3</sup> to  $10^{20}$  cm<sup>3</sup> to study the impact of ETL doping charge density on the PSC efficiency. Figure 8 shows the fluctuation of each device parameter with the donor doping charge concentration of on transport layer. The  $V_{oc}$ , FF and PCE of PSC device parameters significantly increase the doping concentration to  $10^{19}$  cm<sup>3</sup>, but the  $J_{sc}$  slightly reductions with increasing the doping charge concentration to  $10^{20}$  cm<sup>3</sup>. The PSC device parameters rapidly decrease as ETL doping concentration is raised further up to  $10^{20}$  cm<sup>3</sup>. This improvement in device efficiency is caused by the fact that when doping charge concentration rises, the ETLs internal electric field also rises, increasing the charge transport velocity and conductivity (Ghosh et al., 2020). However, excessive doping causes the formation

1 of coulomb traps, which reduces the electron's mobility (Saikia et al., 2022). Therefore, we  
 2 maintain the ETL's optimum donor doping concentration ( $N_D$ ) for future simulations at  $10^{19} \text{ cm}^{-3}$ .  
 3 According to the best PSC efficiency:  $V_{oc} = 1.0249 \text{ V}$ ,  $J_{sc} = 35.2464 \text{ mA/cm}^2$ ,  $FF = 82.47 \%$  and  
 4  $PCE = 29.79 \%$ .

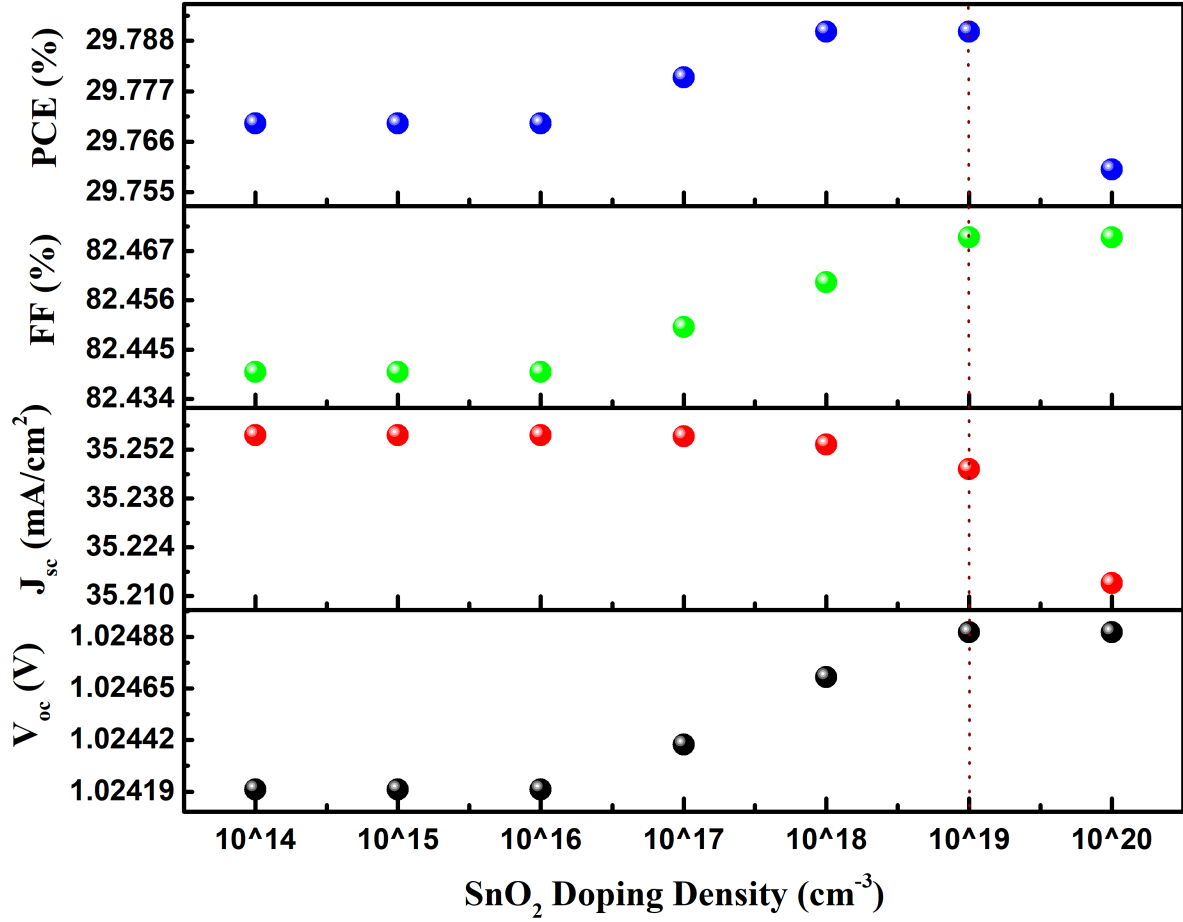


Figure 8 The PSC performance varies depending on the amount of ETL doping.

### 3.5 Optimization of absorber thickness

The PSC performance is determined by the perovskite layer, which creates charge carriers by absorbing light. The thickness of the perovskite layer influences the diffusion lengths and lifetimes of photogenerated holes and electrons. We change the thickness of the MASnBr<sub>3</sub> layer

from 0.1  $\mu\text{m}$  to 1.0  $\mu\text{m}$  to examine the impact of perovskite layer thickness on PSC performance. The J-V characteristics for various absorber thicknesses are illustrated in figure 9. The change in PSC performance relative to absorber ( $\text{MASnBr}_3$ ) thickness is seen in figure 10.  $J_{\text{sc}}$  increase as the perovskite layer thickness increase up to 0.5  $\mu\text{m}$ , then steadily declines as thickness increases. The improvement in JV curve with absorber thickness confirms that the increase in  $J_{\text{sc}}$  is due to a significant amount of photon absorption (Saikia et al., 2022). As absorber thickness increases owing to higher recombination, the dark saturation current is enhanced, which causes  $V_{\text{oc}}$  to fluctuate extremely slowly after a certain value. There is a progressive shift in the system due to the saturation current and recombination rate rise with absorber thickness (Saikia et al., 2022). The FF fluctuates with an increase in thickness. The PCE increases up to 0.5  $\mu\text{m}$  and then slightly linearly decreases with an increase in thickness. Therefore, we select 0.5  $\mu\text{m}$  for future modelling as the ideal  $\text{MASnBr}_3$  thickness. The following is the device performance:  $V_{\text{oc}} = 1.1466 \text{ V}$ ,  $J_{\text{sc}} = 35.1826 \text{ mA/cm}^2$ ,  $\text{FF} = 86.33 \%$ , and  $\text{PCE} = 34.52 \%$ .

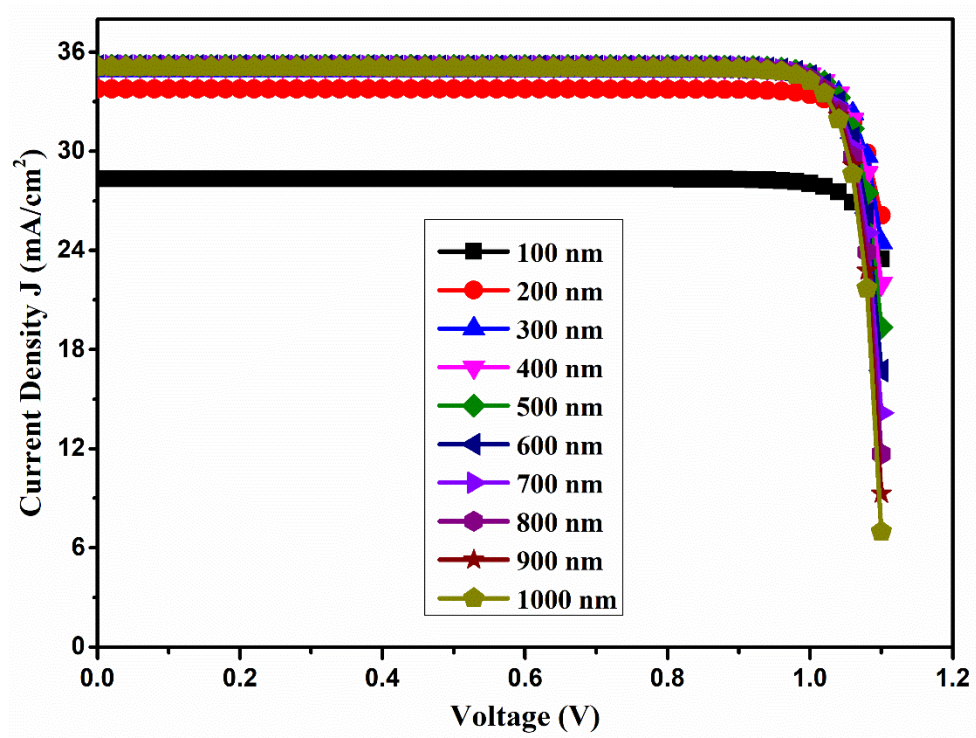


Figure 9 JV curve for perovskite layer at different thickness

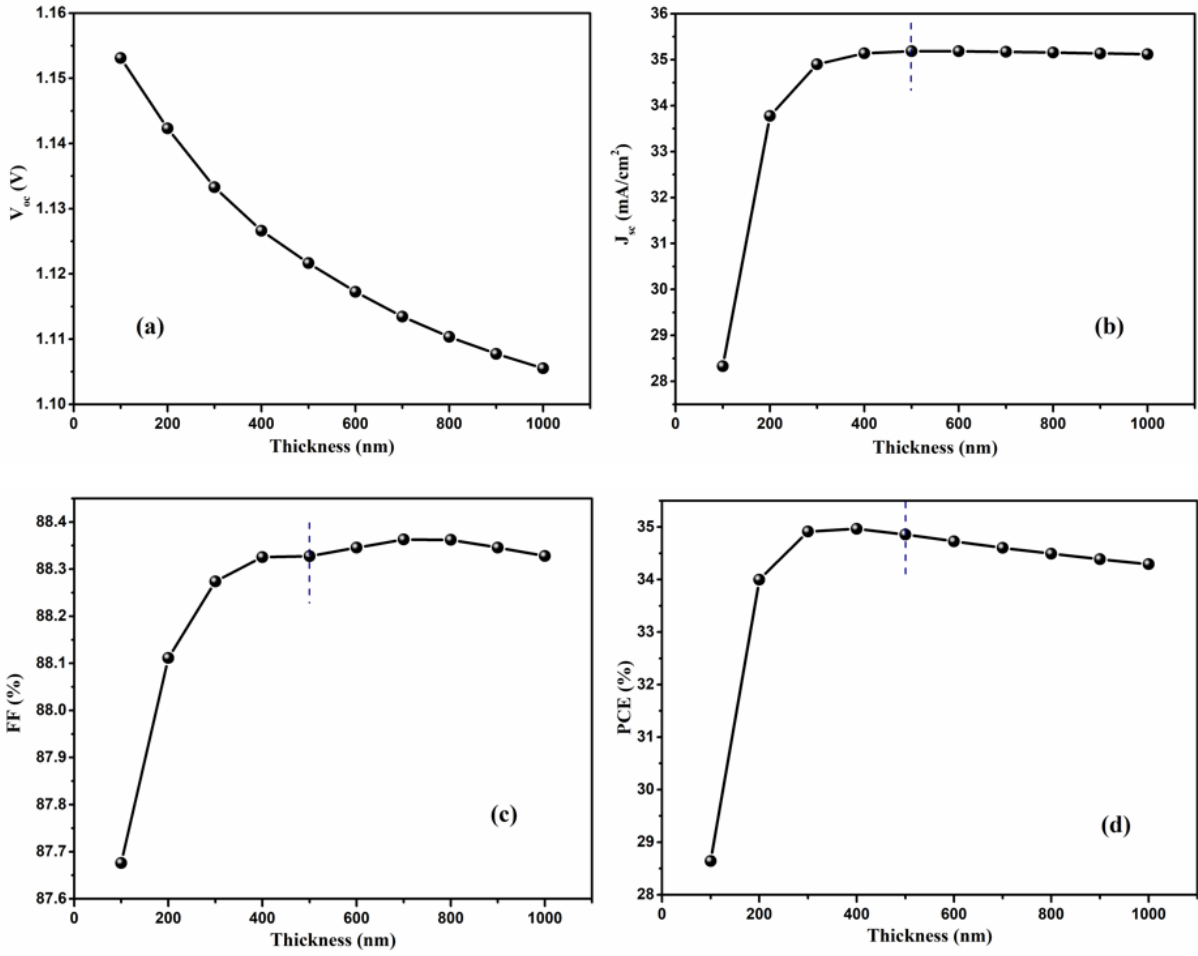


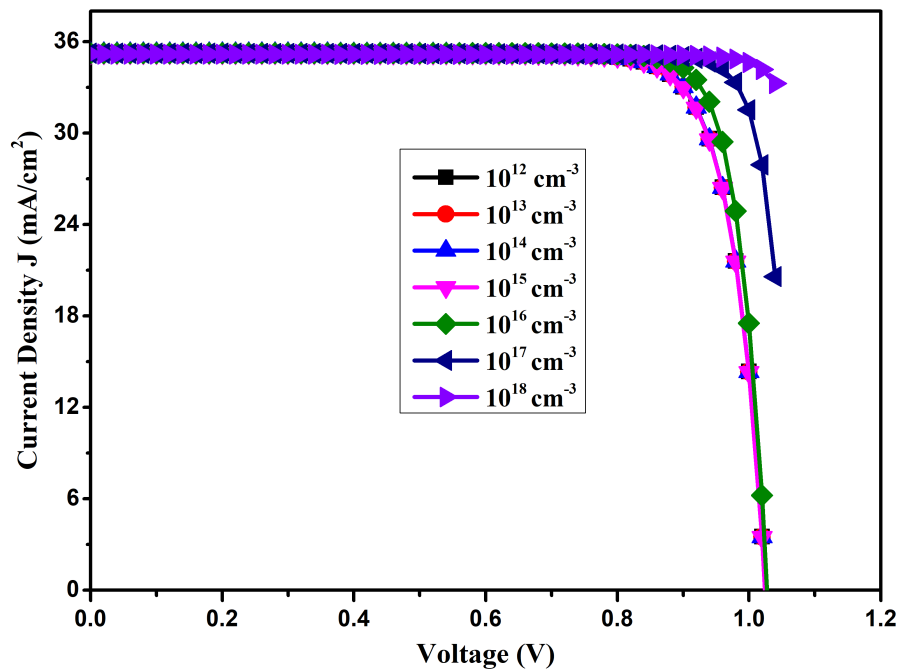
Figure 10 The performance variation of the PSC with the thickness of the perovskite layer

### 3.6 Optimization of Absorber Doping Density

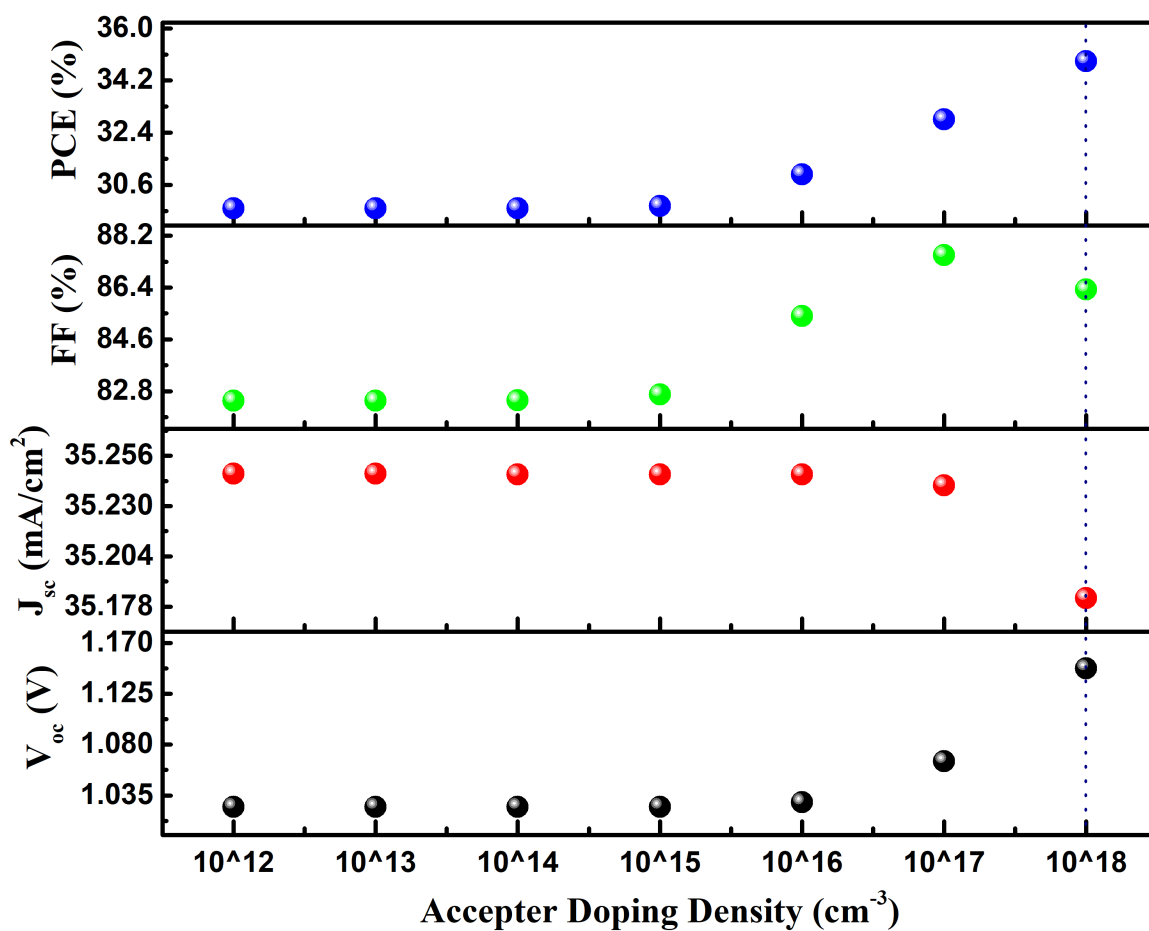
The functionality of the PSC is significantly impacted via the doping of charge transport layers and perovskite material. We initially simulated a perovskite layer with  $10^{16}$  cm<sup>3</sup> of donor and acceptor doping density. We initially simulated the PSC's performance by changing the absorber layer's acceptor concentration between  $10^{12}$  cm<sup>3</sup> and  $10^{18}$  cm<sup>3</sup> to research the impact of doping density on PSC performance. The J-V characteristics for each absorber concentration are shown in figure 11. The fluctuation in PSC performance with acceptor concentration is shown in figure

12. In the presence of  $N_A$  up to  $10^{15} \text{ cm}^3$ ,  $V_{oc}$ ,  $J_{sc}$ , FF, and PCE stay nearly constant. When the concentration of the acceptor doping increases, the  $V_{oc}$ , FF and PCE increase until  $10^{18} \text{ cm}^3$ , and  $J_{sc}$  shows a little reduction until  $10^{18} \text{ cm}^3$  (Saikia et al., 2022). We obtained the best  $V_{oc}$ ,  $J_{sc}$ , FF, and PCE at  $10^{18} \text{ cm}^3$ . To conduct further simulations, we use the  $N_A$  of the perovskite layer of  $10^{18} \text{ cm}^3$ .

We first adjust the  $N_A$  of the perovskite layer before optimizing the donor doping charge concentration ( $N_D$ ). We change the  $N_D$  of the absorber from  $10^{12} \text{ cm}^3$  to  $10^{18} \text{ cm}^3$  to study the impact of  $N_D$  on PSC performance. The J-V characteristics for each donor concentration are shown in figure 13. All the device parameters have linearly increased with increasing the  $N_D$  in the absorber layer, shown in figure 14. It has been noted that  $V_{oc}$ , FF, and PCE stay constant up to  $10^{17} \text{ cm}^3$  before drastically declining, and the  $J_{sc}$  value increased. We obtained the best  $V_{oc}$ ,  $J_{sc}$ , FF, and PCE at  $10^{15} \text{ cm}^3$ . To conduct further simulations, we use the  $N_D$  of the perovskite layer of  $10^{15} \text{ cm}^3$ .



1 Figure 11 JV curve of change the acceptor doping ratio of  $N_A$  in the perovskite layer



2  
3 Figure 12 The PSC performance varies depending on the  $N_A$  doping in the perovskite layer

4

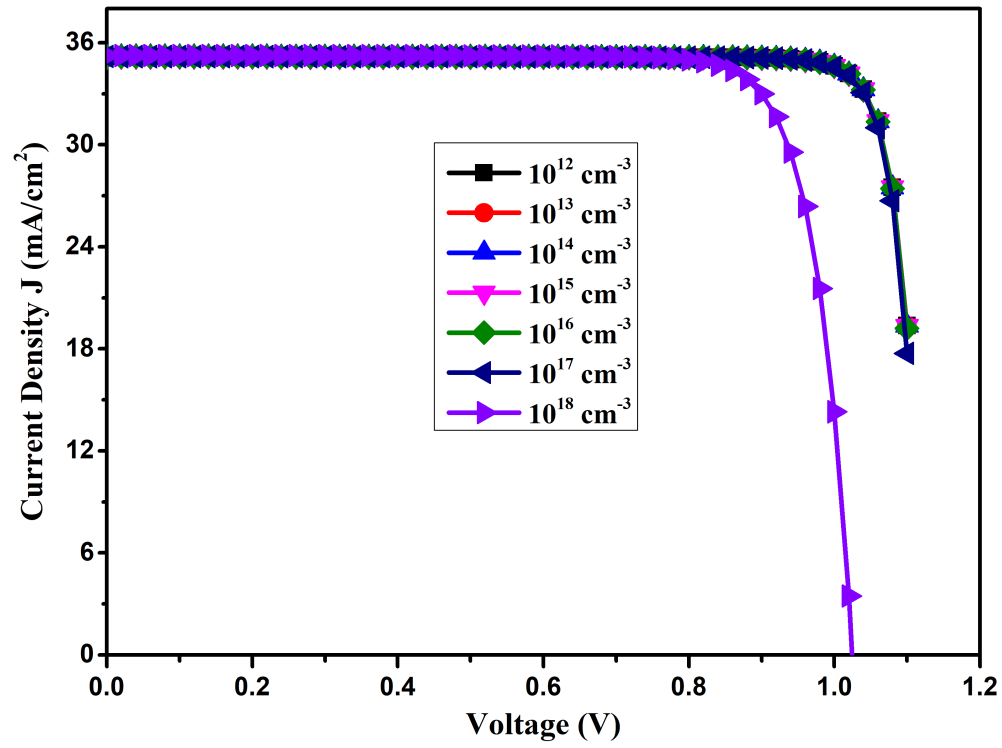


Figure 13 JV curve of change the donor doping ratio of  $N_D$  in the perovskite layer



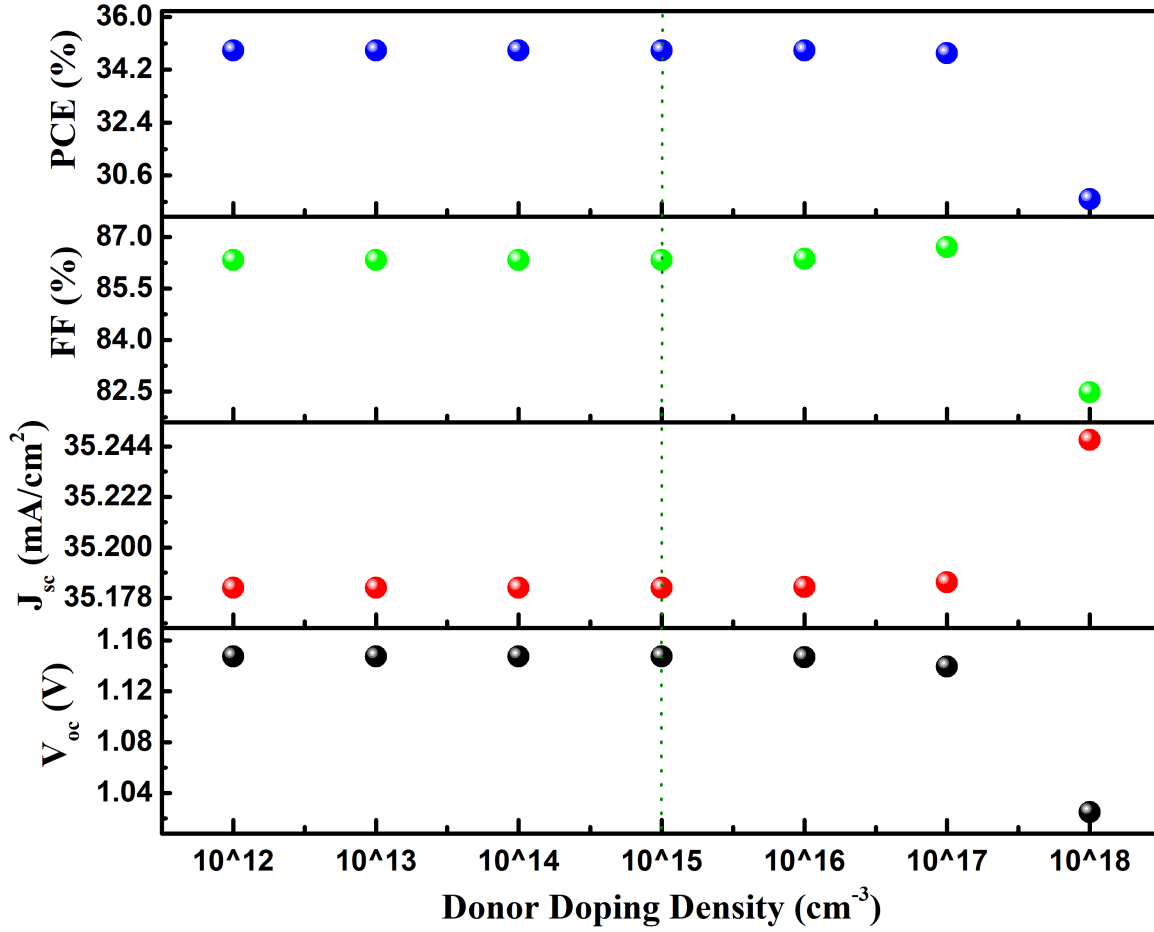


Figure 14 The PSC performance varies depending on the  $N_D$  doping in the perovskite layer

### 3.7 Optimization of absorber defect density

The perovskite layer could have different defects, including interstitials, vacancies, Frenkel and Schottky defects. The perovskite solar cell stability is expressively decreased at large defect amounts (Rai et al., 2020). We calculate the PSC efficiency by changing the absorber defect density ( $N_T$ ) from  $10^{12} \text{ cm}^{-3}$  to  $10^{18} \text{ cm}^{-3}$  to determine the effect of the  $N_T$  on the PSC efficiency.

Figure 15 illustrates the JV characteristics for various  $N_T$  of the perovskite absorber layer. Figure 16 illustrates the fluctuation of the perovskite solar cell IV parameters with changing the  $N_T$  values. The  $J_{sc}$  and PCE are found to fluctuate up to  $10^{15} \text{ cm}^{-3}$ . The  $V_{oc}$  is sharply decreased, and

1 FF is increased up to  $10^{15} \text{ cm}^{-3}$ . After that, all parameter values decrease with further increasing  
2 the  $N_T$  value. The explanation for this loss in performance might be because as the number of  
3 defective sites rises, the possible paths and the number of traps of recombination rise (Johnston  
4 and Herz, 2016). We observed the best PSC performance with device parameters at  $10^{14} \text{ cm}^{-3}$ . To  
5 conduct further simulations, we use the  $N_T$  of the perovskite layer of  $10^{14} \text{ cm}^{-3}$ .

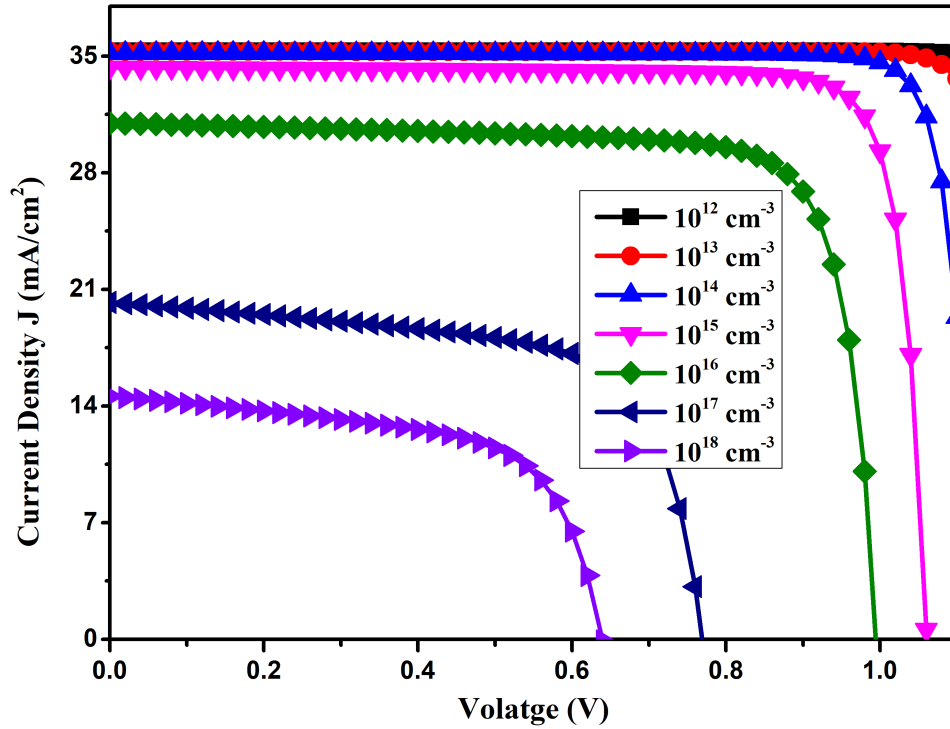


Figure 15 J-V curves for various absorber defect concentrations

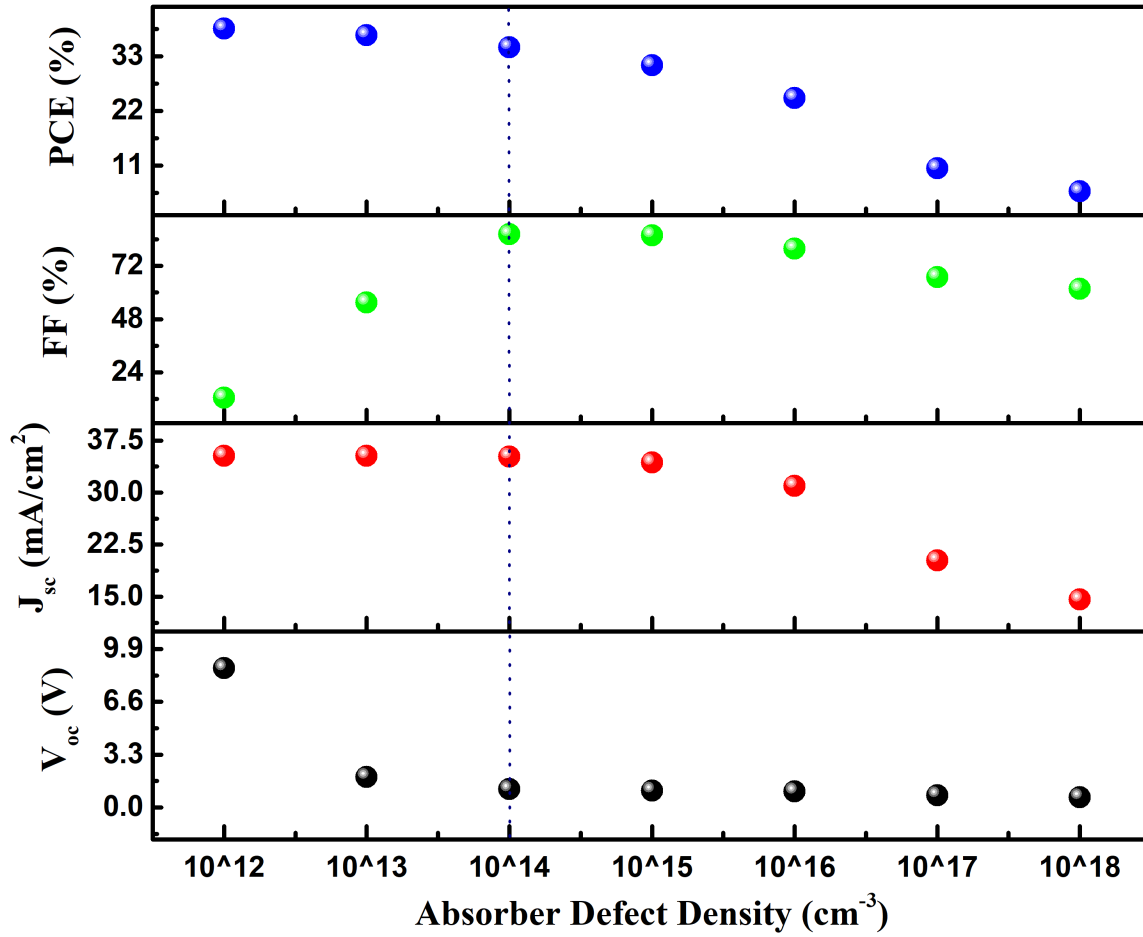
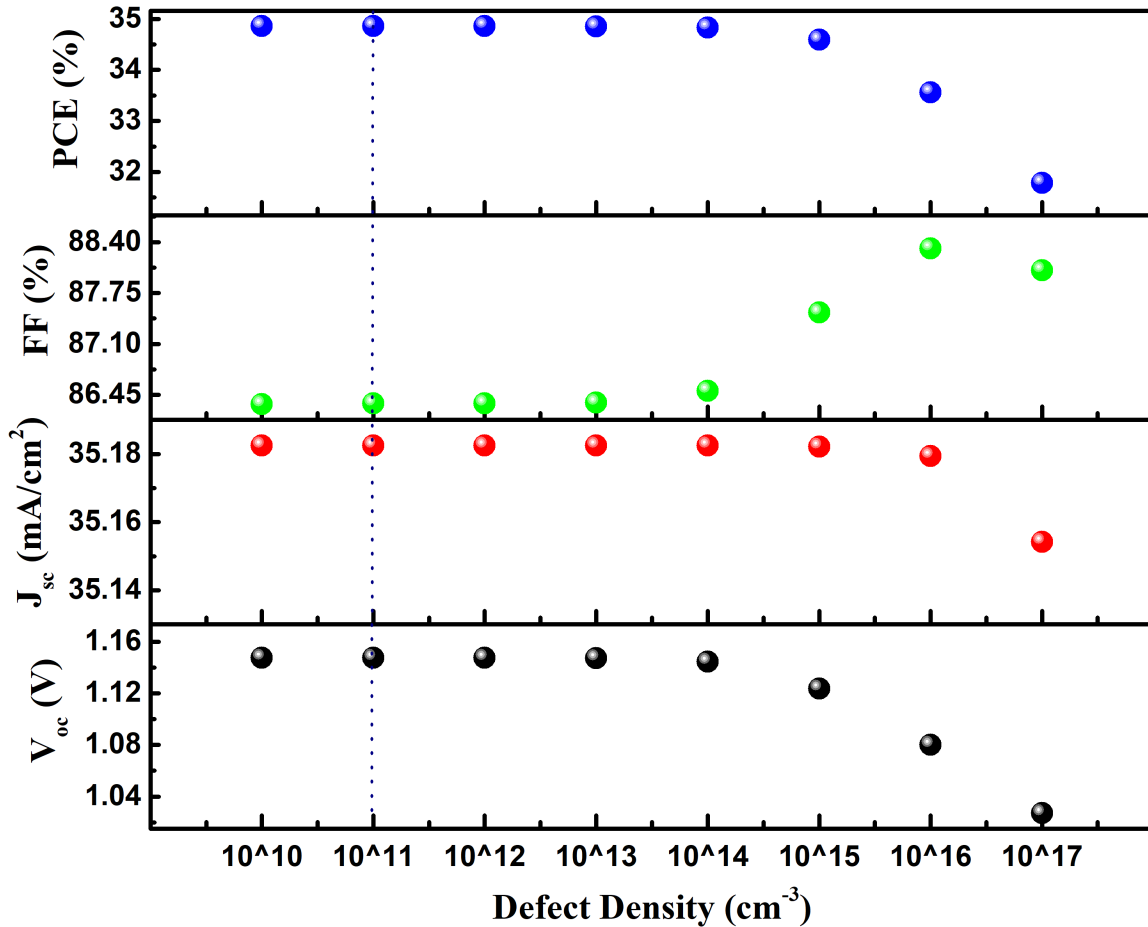


Figure 16 Variation in PSC performance as a function of absorber defect density

### 3.8 Optimization of the ETL/perovskite interface defect density

We added interface fault density to our baseline simulation to simulate more realistic conditions. The defect density impacts the PSC's efficiency and stability at the ETL/absorber contact. We simulate the PSC efficiency by changing the defect density at the interface of ETL/perovskite from  $10^{10} \text{ cm}^{-3}$  to  $10^{17} \text{ cm}^{-3}$  to evaluate the impact of the interface ETL/perovskite defect density on the PSC performance. Where the defect state position has been taken into consideration to be in the centre of the contact with a uniform energy distribution. Figure 17 illustrates the perovskite solar cell IV parameters with changing interface ETL/perovskite defect density

1 values. All the PSC device parameters are linearly increased, increasing the defect density to  $10^{13}$   
 2  $\text{cm}^{-3}$ . The  $V_{\text{oc}}$ ,  $J_{\text{sc}}$  and PCE are decreased with a further increase in the interface defect density,  
 3 but FF is increased. The decline in PSC performance may be brought about by the fact that when  
 4 the defect density at the ETL/perovskite interface increases, there is a greater chance that  
 5 electrons travel from the perovskite layer to the ETL may be trapped, recombined or scattered.  
 6 While  $10^{11} \text{ cm}^{-3}$  delivers the optimum performance based on our data, thus we chose this value  
 7 for the ETL/perovskite defect density for further simulation. The following is the PSC  
 8 performance:  $V_{\text{oc}} = 1.1214 \text{ V}$ ,  $J_{\text{sc}} = 34.8614 \text{ mA/cm}^2$ ,  $\text{FF} = 88.30 \%$ , and  $\text{PCE} = 34.52 \%$ .



9

10 Figure 17 The PSC performance variation with an interface defect density of ETL/perovskite

### 3.9 Optimization of the perovskite/HTL interface defect density

We increased the number of interface defects in our original simulation for different simulation results. The defect density impacts the PSC efficiency and stability at the interference of perovskite/HTL. We calculate the device efficiency by changing the defect density at the interface layer of perovskite/HTL from  $10^{10} \text{ cm}^{-3}$  to  $10^{20} \text{ cm}^{-3}$  to estimate the effect of the interface perovskite/HTL defect density on the PSC efficiency. Where the defect state position is assumed to be in the centre of the contact with uniform energy distribution. Figure 18 illustrates the perovskite solar cell IV parameters with changing interface perovskite/HTL defect density values. All the PSC device parameters are linearly increased, increasing the defect density to  $10^{12} \text{ cm}^{-3}$ . The  $V_{oc}$ ,  $J_{sc}$  and PCE are decreased with a further increase in the interface defect density, but FF is increased. The decline in PSC performance may be brought about by the fact that when the defect density at the perovskite/HTL interface increases, there is a greater chance that hole travel from the perovskite layer to the HTL may be trapped, recombined or scattered. While  $10^{12} \text{ cm}^{-3}$  delivers the optimum performance based on our data, thus we chose this value for the perovskite/HTL defect density for further simulation. The following is the device efficiency:  $V_{oc} = 1.1391 \text{ V}$ ,  $J_{sc} = 35.1655 \text{ mA/cm}^2$ ,  $FF = 86.76 \%$ , and  $PCE = 34.45 \%$ .

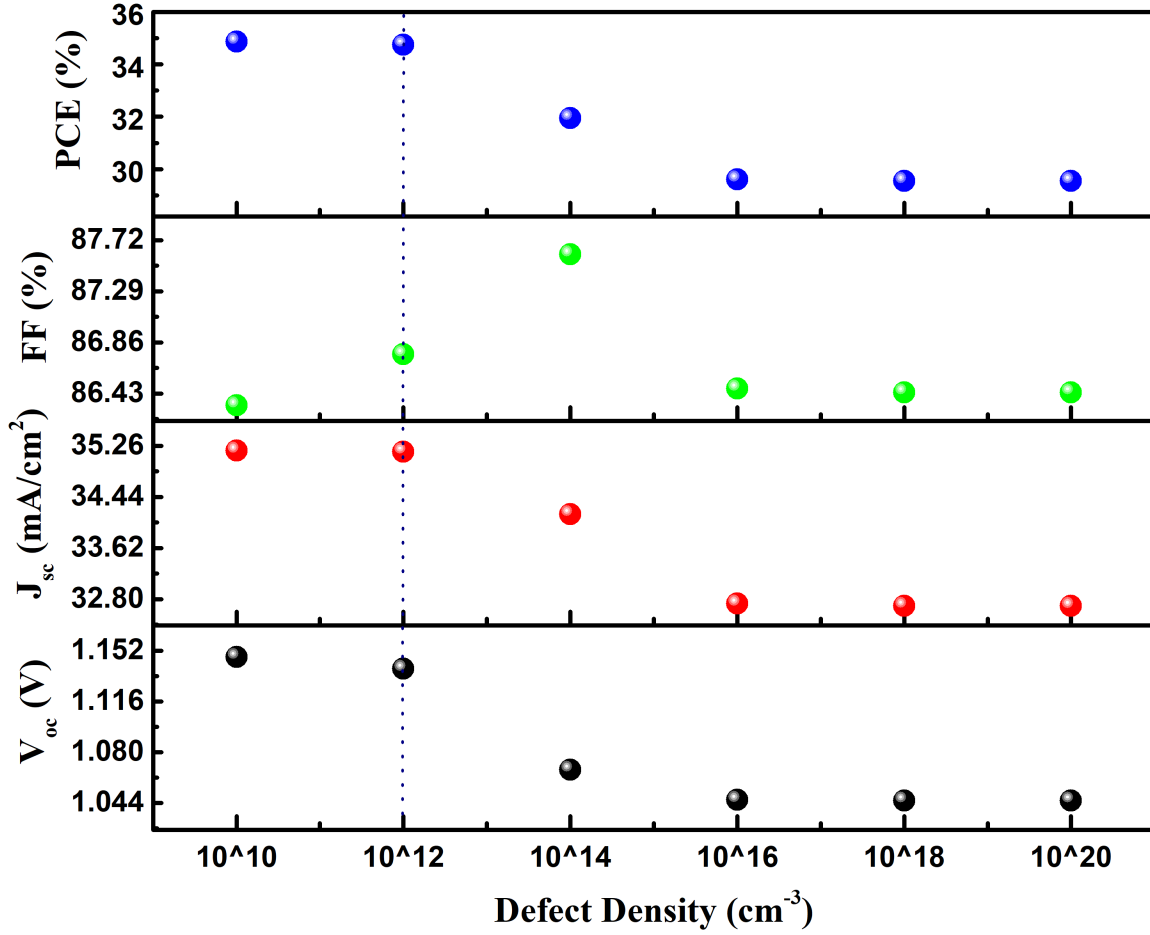


Figure 18 The PSC performance variation with an interface defect density of perovskite/HTL

### 3.10 Optimization of Suitable Work Function

The work function of the suitable back contact plays a vital role in the PSC performance and stability. We calculate the PSC efficiency with various back contacts to investigate the impact of the suitable back contact function on PSC efficiency. The back contacts employed in this investigation have the following work functions: Cu (4.6 eV), Ag (4.7 eV), Fe (4.8 eV), Au (5.1 eV), C (5.0 eV), W (5.22 eV) and Ni (5.35 eV) (Saikia et al., 2022). The  $V_{oc}$ ,  $J_{sc}$ , FF and PCE of the perovskite solar cell with various back contact working functions are illustrated in figure 19.

The optimized structure of the  $V_{oc}$ ,  $J_{sc}$ , FF and PCE parameters are relatively low in the back

contact work function range (4.6-4.9). The PSC performance is the best in the back contact work function range (5.0-5.4). So the Au (5.1 eV), C (5.0 eV), W (5.22 eV) and Ni (5.35 eV) are observed as the best  $V_{oc}$ ,  $J_{sc}$ , FF and PCE parameters. We have optimized and used the Au back contact for the final device

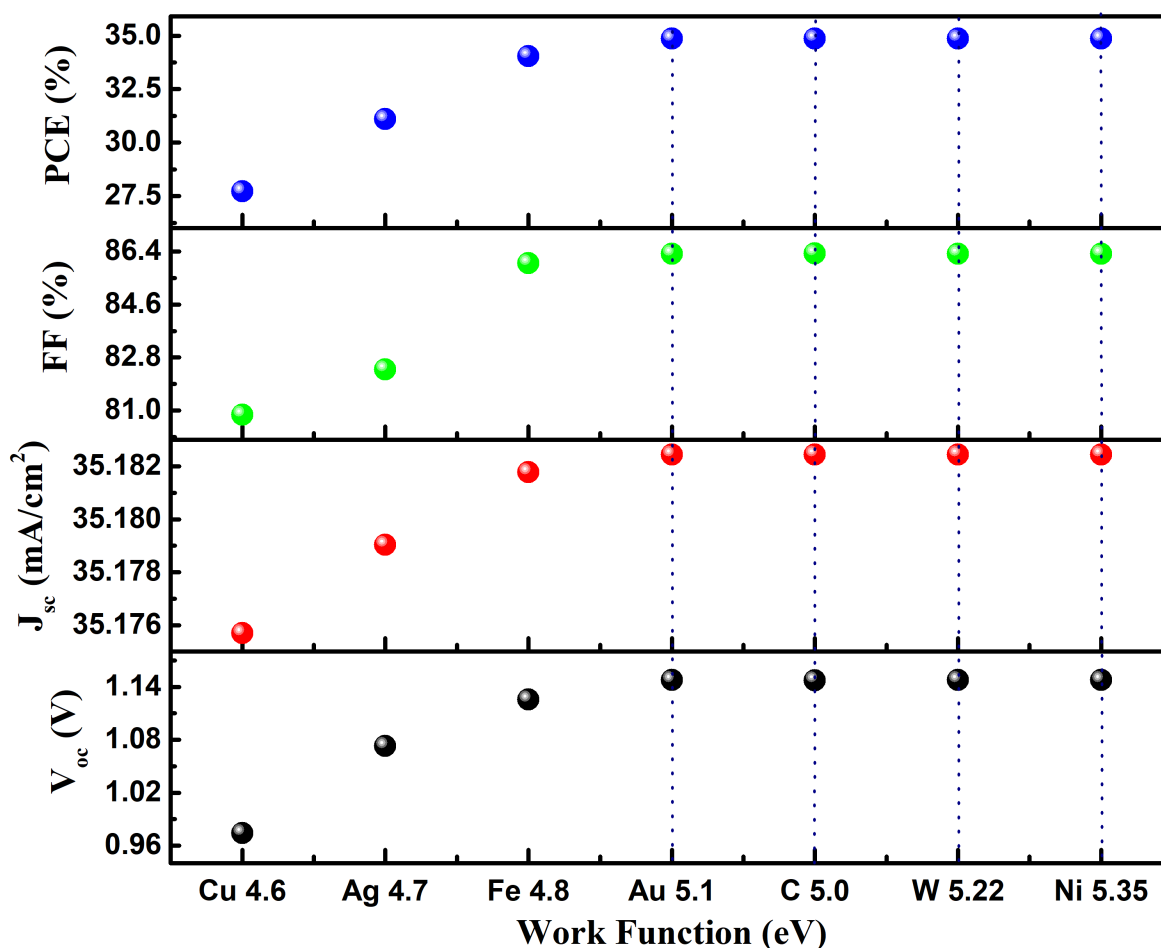


Figure 19 The PSC device performance with the different back contact

### 3.11 Device Performance affected via Series Resistance

The rear contact (Au), HTL (NiO), perovskite (MASnBr<sub>3</sub>) layer, ETL (SnO<sub>2</sub>), and front contact (FTO) provide the device's electrical resistance. To investigate the influence of series resistance on device efficiency, we simulate PSC efficiency while adjusting the series resistance range from

1 (0-10)  $\Omega \text{ cm}^2$ . Figure 20 depicts the J-V curve for various series resistances. The fluctuation in IV  
 2 parameters with series resistance is seen in figure 21. The  $V_{OC}$  remains constant as series  
 3 resistance rises, but  $J_{sc}$ , FF, and PCE fall as series resistance rise. Therefore, improved  
 4 performance is achieved with a low degree of series resistance. Therefore, we determine that 1  
 5  $\Omega \text{ cm}^2$  is the excellent series resistance.

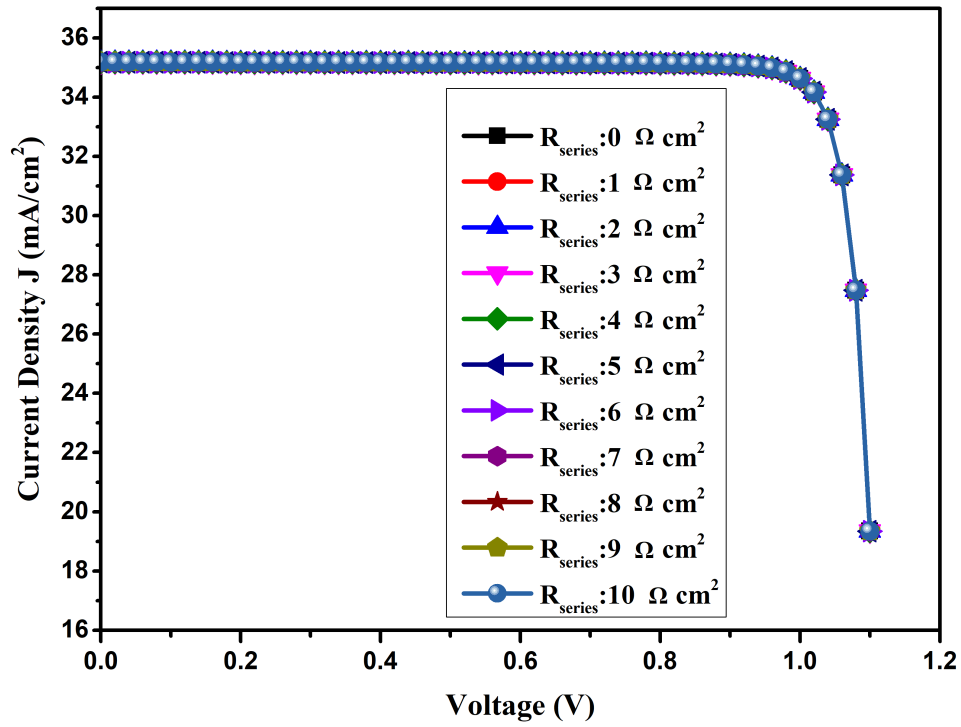


Figure 20 J-V curves for various series resistances.



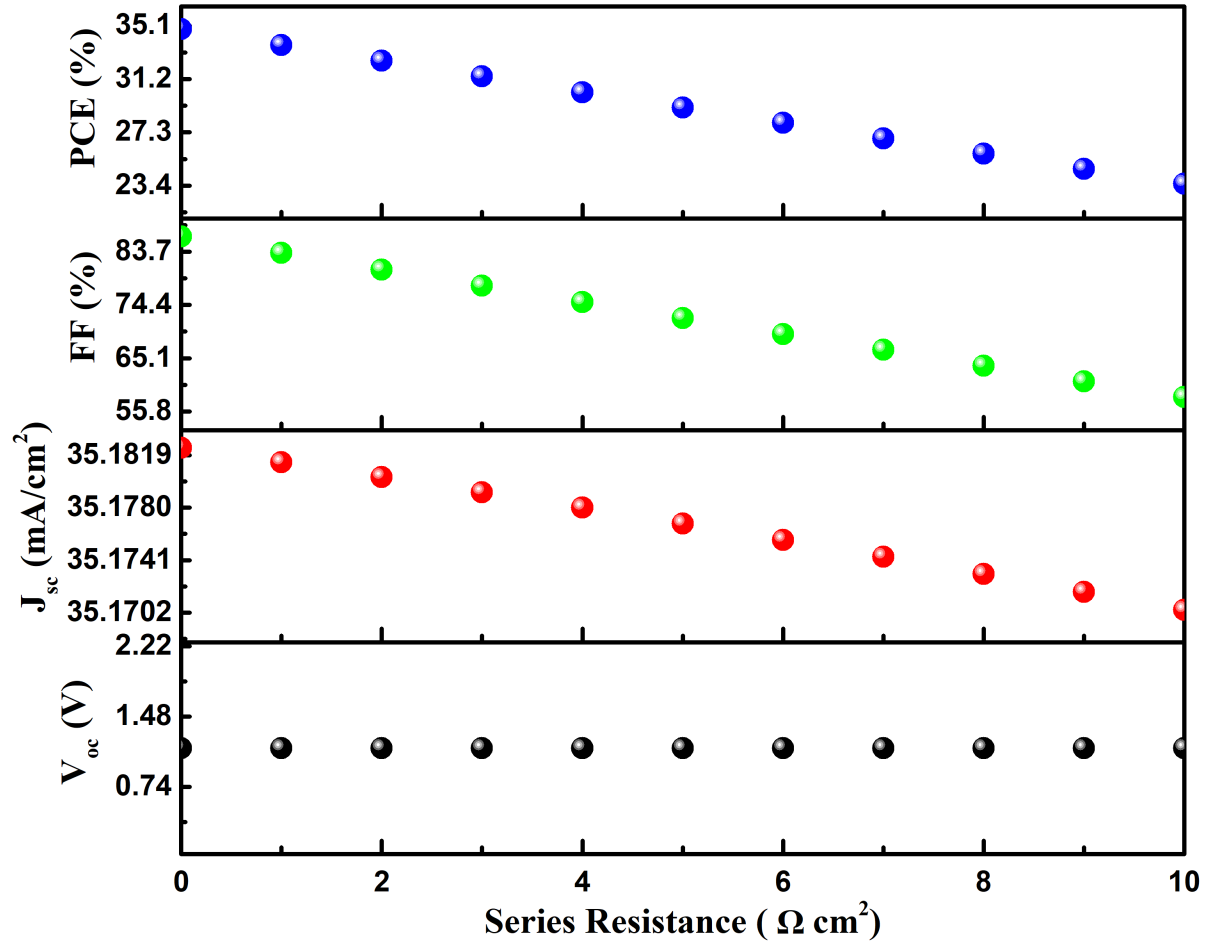


Figure 21 The PSC performance of the variation with different series resistance

### 3.12 Device Performance affected via Shunt Resistance

Shunt resistance develops in the PSC through various charge recombination pathways (Saikia et al., 2022). To investigate the influence of shunt resistance on PSC efficiency, we simulate PSC efficiency while adjusting the shunt resistance range from (1000-7000)  $\text{cm}^2$ . Figure 22 depicts the J-V curve for various shunt resistances. The fluctuation in IV parameters with shunt resistance is seen in figure 23. The  $J_{sc}$  remains constant as series resistance rises, but  $V_{oc}$ , FF, and PCE linearly increase as series resistance rise. Therefore, improved performance is achieved with

- 1 a high degree of shunt resistance. Therefore, we found that 7000  $\Omega \text{ cm}^2$  is the excellent shunt
- 2 resistance. At 7000  $\Omega \text{ cm}^2$ , we achieved the FF = 88 % and PSC = 34.41 %.

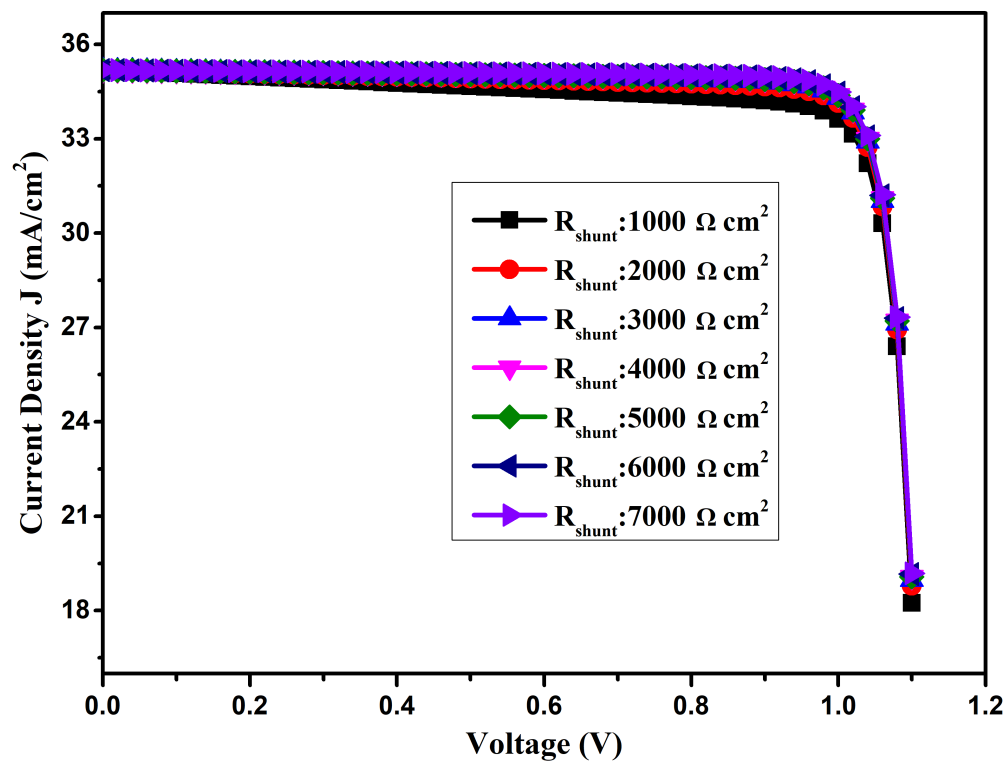


Figure 22 J-V curves for various shunt resistances.

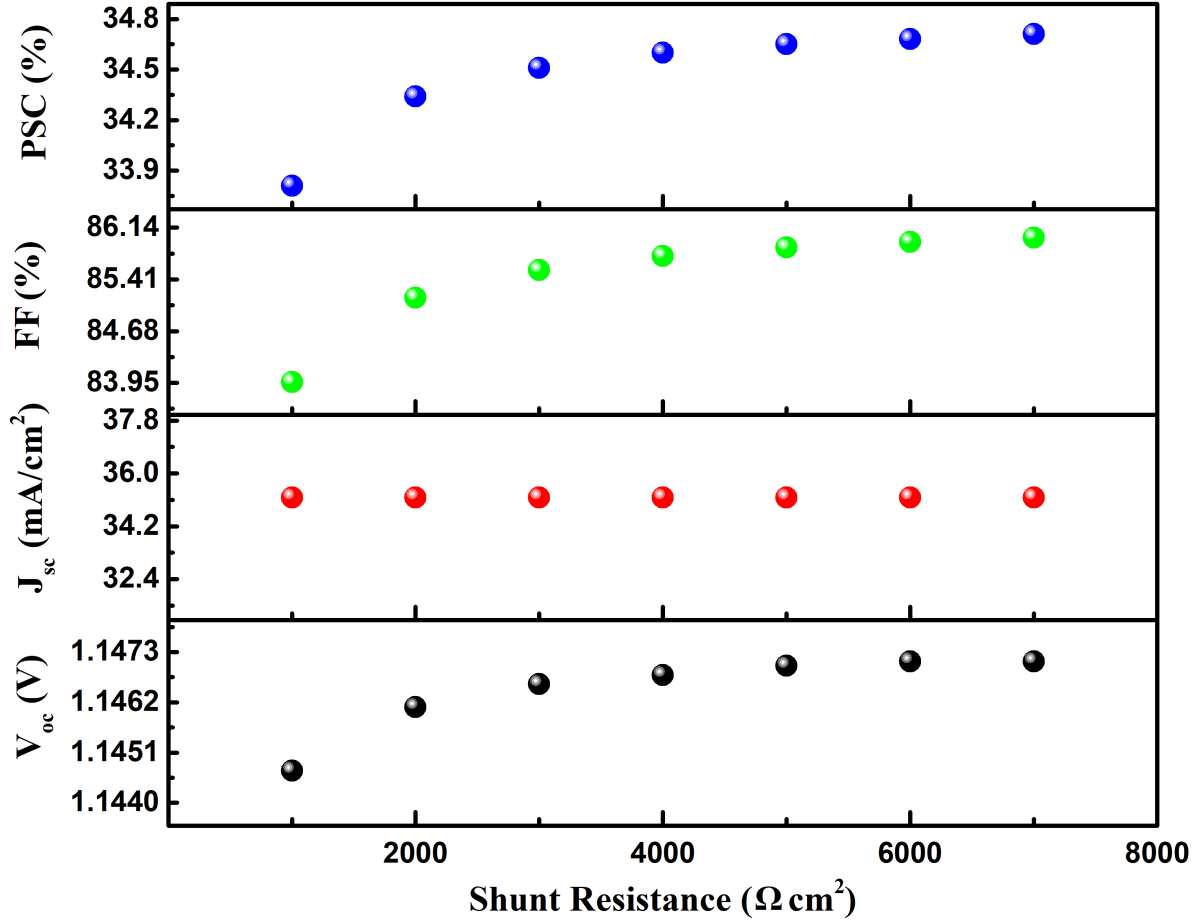


Figure 23 Variation of PSC performance with different shunt resistance.

### 3.13 Optimized Device Performance

The physical characteristics of the enhanced device are shown in Table 6. The optimized device structure and its energy level diagram are shown in figure 24. The QE wavelength and JV curve for the optimized PSC performance are shown in figure 25. The optimized PSC performance has a defect density ( $10^{15} \text{ cm}^{-2}$ ), the interface at ETL/perovskite ( $10^{11} \text{ cm}^{-2}$ ) and interfaces at perovskite/HTL ( $10^{12} \text{ cm}^{-2}$ ). The optimum PSC efficiency is as follows:  $V_{oc} = 1.1214 \text{ V}$ ,  $J_{sc} = 34.8414 \text{ mA/cm}^2$ ,  $FF = 88.30 \%$ , and  $PCE = 34.52 \%$ .

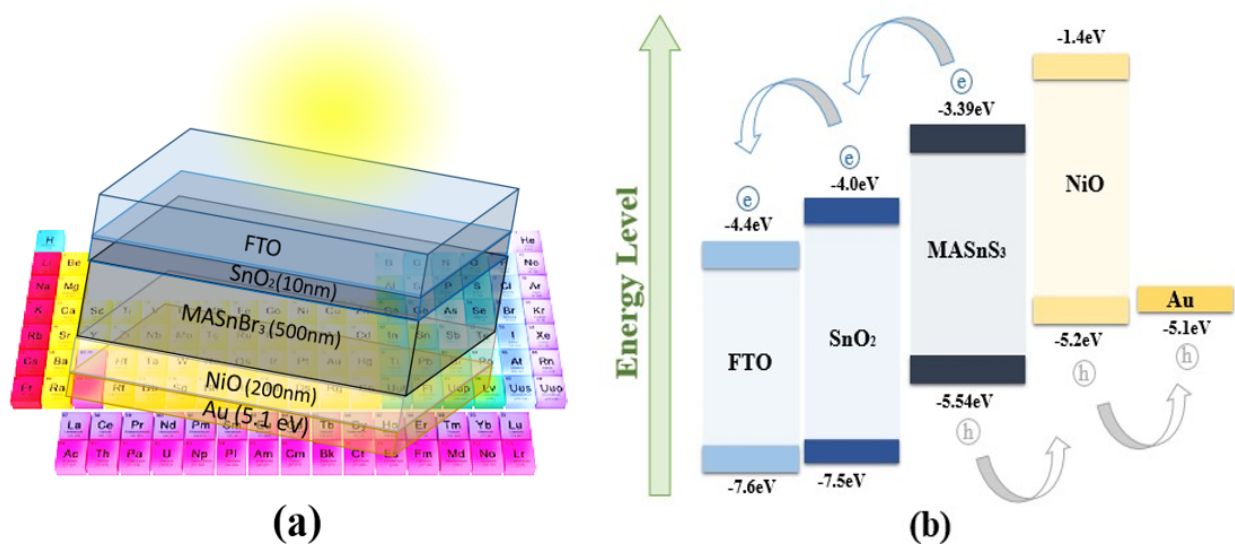


Figure 24 (a) optimized perovskite solar cell structure and its (b) energy level

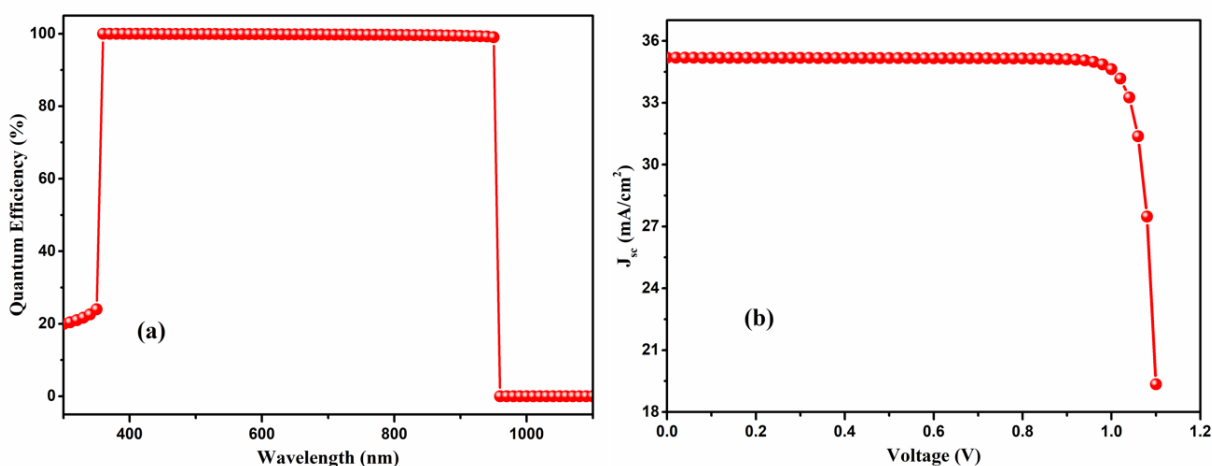
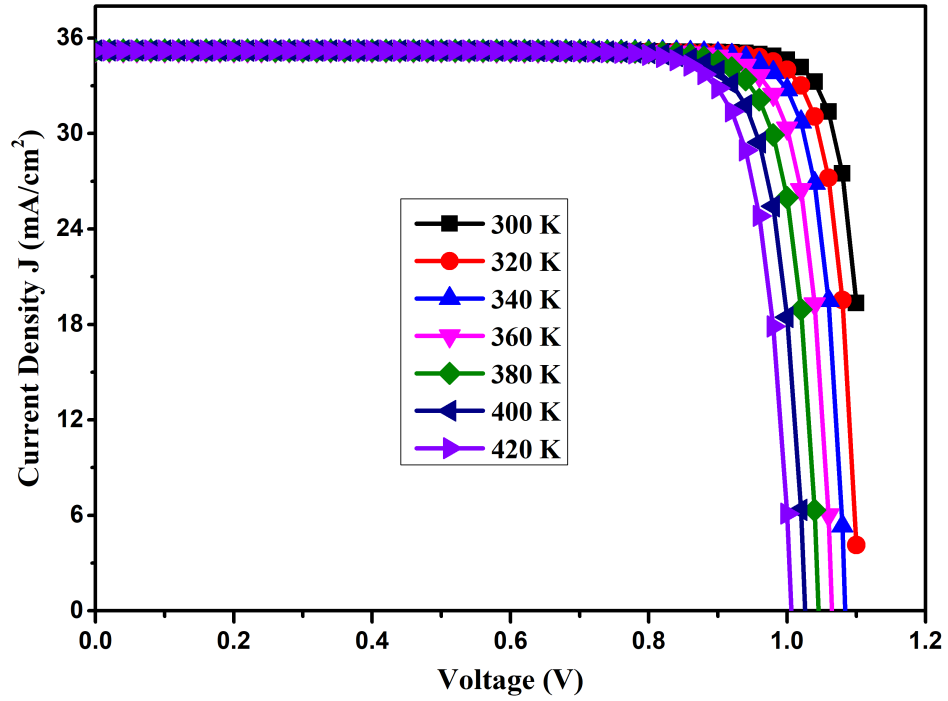


Figure 25 the optimized perovskite solar cell (a) QE wavelength curve (b) JV curve

### 3.14 Effect of temperature on PSC performance

We study the optimized PSC efficiency of the perovskite solar cell by varying the temperature from 300 K to 420 K. The JV curve of enhanced perovskite solar cell structure at different temperatures is shown in figure 26. The PSC device efficiency, such as  $V_{oc}$ ,  $J_{sc}$ , FF and PCE

1 variation with rising temperature, is seen in figure 27. The  $V_{OC}$ , FF, and PCE all decrease as  
 2 temperature rises, but the  $J_{sc}$  increases as the temperature increases. The reason for this drop in  
 3 performance is that when the temperature rises, the recombination rate and saturation current rise  
 4 as well (Ahmed et al., 2021).



5  
 6 Figure 26 shows the JV curve of optimized perovskite solar cell at different temperature

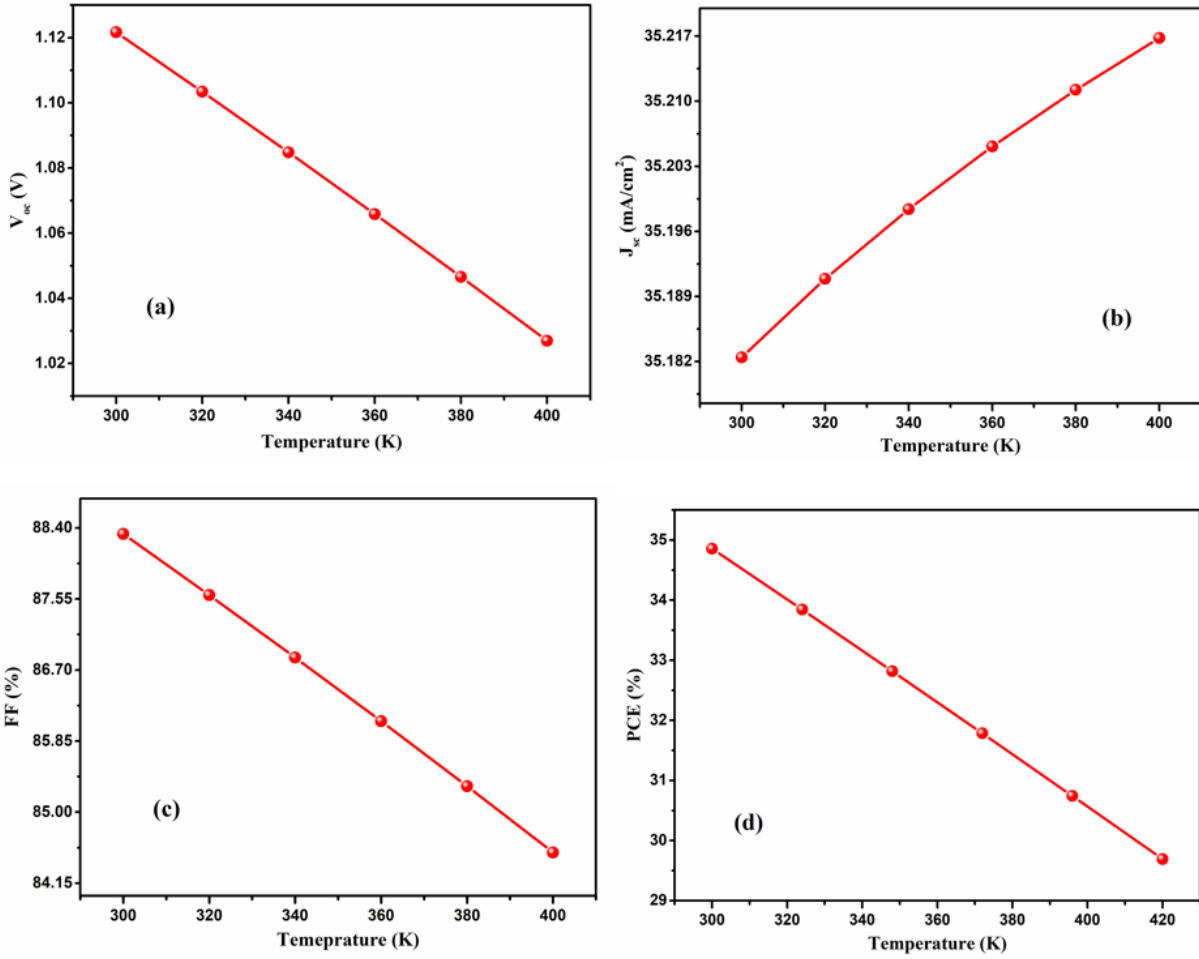


Figure 27 The optimized perovskite solar cell performance at different temperature

Table 6 The optimized device SCAPS-1D input parameters

Properties	NiO	MASnBr <sub>3</sub>	TiO <sub>2</sub>	FTO
d (μm)	0.200	0.500	0.01	0.40
E <sub>g</sub> (eV)	3.600	1.30	3.3	3.50
χ (eV)	1.800	4.17	4	4.00
ε <sub>r</sub> (eV)	11.70	10	9	9.00
N <sub>C</sub> (1/cm <sup>3</sup> )	2.5×10 <sup>20</sup>	2.2×10 <sup>18</sup>	2.2×10 <sup>17</sup>	2.2×10 <sup>18</sup>
N <sub>V</sub> (1/cm <sup>3</sup> )	2.5×10 <sup>20</sup>	1.8×10 <sup>18</sup>	2.2×10 <sup>16</sup>	1.8×10 <sup>18</sup>
μ <sub>e</sub> (cm <sup>2</sup> /Vs)	2.8×10 <sup>0</sup>	1.6×10 <sup>0</sup>	2.00×10 <sup>2</sup>	2.0×10 <sup>1</sup>

$\mu_p$ (cm <sup>2</sup> /Vs)	$2.8 \times 10^0$	$1.6 \times 10^0$	$8.00 \times 10^1$	$1.0 \times 10^1$
$N_D$ (1/cm <sup>3</sup> )	0	$1.00 \times 10^{15}$	$1.00 \times 10^{19}$	$1.0 \times 10^{19}$
$N_A$ (1/cm <sup>3</sup> )	$3.00 \times 10^{20}$	$1.00 \times 10^{18}$	0	0
$N_T$ (1/cm <sup>3</sup> )	$1.00 \times 10^{14}$	$1.00 \times 10^{14}$	$1.00 \times 10^{15}$	$1.0 \times 10^{14}$

#### 4. Conclusion

In this study, lead-free perovskite solar cells with the perovskite layer (MASnBr<sub>3</sub>) are modelled, and their performance is analyzed using the SCAPS 1D software. TiO<sub>2</sub>, SnO<sub>2</sub>, ZnO, CdS, and Spiro-OMeTAD are used as ETLs, Cu<sub>2</sub>O, CuSbS<sub>2</sub>, CuI, WS<sub>2</sub>, and NiO are used as HTLs, Au, C, W, Ni, Ag, Fe, and Cu are used as back contact. The performance study and modelling of lead-free MASnBr<sub>3</sub>-based planar heterojunction cells show the parameters of the HTLs, ETLs, the absorber layer, interface layers and the work function of the selected back contact metals have a significant impact on the efficiency of the PSC. The maximal device performance may be attained by carefully choosing the back metal contacts and adjusting the perovskite material properties, such as defect density, thickness, acceptor and donor dopant concentration. The optimal device performance is significantly influenced by temperature. This simulation and modelling study shows the highest efficiency has achieved via cell configuration glass/FTO/SnO<sub>2</sub>/MASnBr<sub>3</sub>/NiO/Au with  $V_{oc} = 1.1214$  V,  $J_{sc} = 34.8614$  mA/cm<sup>2</sup>, FF = 88.30 %, and PCE = 34.52 %. The perovskite layer thickness significantly influences the device efficiency of lead-free PSC. The best efficiency is attained with a standard thin perovskite layer of thickness of 500 nm. The analysis of the device configuration reveals that the device configuration is stable at 300 K, and the IV parameters of PSC efficiency gradually decline with temperature.

#### Acknowledgment

The authors would like to acknowledge the British Council for their funding under PAK-UK ICRG 2020 project (006327/D/ISB/008/2021) to create a research group of MS, Ph.D and Postdoctoral students and establishment of "Semiconductor Physics and Renewable Energy Laboratory" (SPREL) at Government College University Faisalabad Pakistan.

## Reference

Ahmed, S., Jannat, F., Khan, M.A.K., Alim, M.A., 2021. Numerical development of eco-friendly  $\text{Cs}_2\text{TiBr}_6$  based perovskite solar cell with all-inorganic charge transport materials via SCAPS-1D. Optik 225, 165765.

Al-Douri, Y., Hashim, U., Khenata, R., Reshak, A., Ameri, M., Bouhemadou, A., Ruslinda, A.R., Arshad, M.M., 2015. Ab initio method of optical investigations of  $\text{CdS}_{1-x}\text{Te}_x$  alloys under quantum dots diameter effect. Solar Energy 115, 33-39.

Anwar, F., Mahbub, R., Satter, S.S., Ullah, S.M., 2017. Effect of different HTM layers and electrical parameters on ZnO nanorod-based lead-free perovskite solar cell for high-efficiency performance. International Journal of Photoenergy 2017.

Ashfaq, A., Jacob, J., Bano, N., Nabi, M.A.U., Ali, A., Ahmad, W., Mahmood, K., Arshad, M., Ikram, S., Rehman, U., 2019. A two step technique to remove the secondary phases in CZTS thin films grown by sol-gel method. Ceramics International 45(8), 10876-10881.

Devi, C., Mehra, R., 2019. Device simulation of lead-free  $\text{MASnI}_3$  solar cell with  $\text{CuSbS}_2$  (copper antimony sulfide). Journal of materials science 54(7), 5615-5624.

Eperon, G.E., Stranks, S.D., Menelaou, C., Johnston, M.B., Herz, L.M., Snaith, H.J., 2014. Formamidinium lead trihalide: a broadly tunable perovskite for efficient planar heterojunction solar cells. Energy Environmental Science 7(3), 982-988.



1 Ghosh, A., Dipta, S.S., Nikor, S.S.S., Saqib, N., Saha, A., 2020. Performance analysis of an  
2 efficient and stable perovskite solar cell and a comparative study of incorporating metal oxide  
3 transport layers. *JOSA B* 37(7), 1966-1973.

4 Gu, Y.-F., Du, H.-J., Li, N.-N., Yang, L., Zhou, C.-Y., 2019. Effect of carrier mobility on  
5 performance of perovskite solar cells. *Chinese Physics B* 28(4), 048802.

6 Hima, A., Lakhdar, N., 2020. Enhancement of efficiency and stability of  $\text{CH}_3\text{NH}_3\text{GeI}_3$  solar cells  
7 with  $\text{CuSbS}_2$ . *Optical Materials* 99, 109607.

8 Jayan, K.D., Sebastian, V., 2021. Comprehensive device modelling and performance analysis of  
9  $\text{MASnI}_3$  based perovskite solar cells with diverse ETM, HTM and back metal contacts. *Solar*  
10 *Energy* 217, 40-48.

11 Johnston, M.B., Herz, L.M., 2016. Hybrid perovskites for photovoltaics: charge-carrier  
12 recombination, diffusion, and radiative efficiencies. *Accounts of chemical research* 49(1), 146-  
13 154.

14 Ju, M.-G., Chen, M., Zhou, Y., Dai, J., Ma, L., Padture, N.P., Zeng, X.C., 2018. Toward eco-  
15 friendly and stable perovskite materials for photovoltaics. *Joule* 2(7), 1231-1241.

16 Kazim, S., Nazeeruddin, M.K., Grätzel, M., Ahmad, S., 2014. Perovskite as light harvester: a  
17 game changer in photovoltaics. *Angewandte Chemie International Edition* 53(11), 2812-2824.

18 Khadka, D.B., Shirai, Y., Yanagida, M., Miyano, K., 2018. Degradation of encapsulated  
19 perovskite solar cells driven by deep trap states and interfacial deterioration. *Journal of Materials*  
20 *Chemistry C* 6(1), 162-170.

21 Kolaczowski, B., Thornton, J.W., 2004. Performance of maximum parsimony and likelihood  
22 phylogenetics when evolution is heterogeneous. *Nature* 431(7011), 980-984.

1 Kour, R., Arya, S., Verma, S., Gupta, J., Bandhoria, P., Bharti, V., Datt, R., Gupta, V., 2019.  
2 Potential substitutes for replacement of lead in perovskite solar cells: A review. Global  
3 Challenges 3(11), 1900050.

4 Lakhdar, N., Hima, A., 2020. Electron transport material effect on performance of perovskite  
5 solar cells based on  $\text{CH}_3\text{NH}_3\text{GeI}_3$ . Optical Materials 99, 109517.

6 Liu, F., Zhu, J., Wei, J., Li, Y., Lv, M., Yang, S., Zhang, B., Yao, J., Dai, S., 2014. Numerical  
7 simulation: toward the design of high-efficiency planar perovskite solar cells. Applied Physics  
8 Letters 104(25), 253508.

9 Lv, Y., Yuan, R., Cai, B., Bahrami, B., Chowdhury, A.H., Yang, C., Wu, Y., Qiao, Q., Liu, S.,  
10 Zhang, W.H., 2020. High-Efficiency Perovskite Solar Cells Enabled by Anatase  $\text{TiO}_2$   
11 Nanopyramid Arrays with an Oriented Electric Field. Angewandte Chemie 132(29), 12067-  
12 12074.

13 Mandadapu, U., Vedanayakam, S.V., Thyagarajan, K., Reddy, M.R., Babu, B., 2017. Design and  
14 simulation of high efficiency tin halide perovskite solar cell. Int. J. Renew. Energy Res 7(4),  
15 1603-1612.

16 McMeekin, D.P., Sadoughi, G., Rehman, W., Eperon, G.E., Saliba, M., Hörlantner, M.T.,  
17 Haghighirad, A., Sakai, N., Korte, L., Rech, B., 2016. A mixed-cation lead mixed-halide  
18 perovskite absorber for tandem solar cells. Science 351(6269), 151-155.

19 Pindolia, G., Shinde, S.M., Jha, P.K., 2022. Optimization of an inorganic lead free  $\text{RbGeI}_3$  based  
20 perovskite solar cell by SCAPS-1D simulation. Solar Energy 236, 802-821.

21 Rai, S., Pandey, B., Dwivedi, D.J.O.M., 2020. Modeling of highly efficient and low cost  
22  $\text{CH}_3\text{NH}_3\text{Pb}(\text{I}_{1-x}\text{Cl}_x)_3$  based perovskite solar cell by numerical simulation. 100, 109631.

- 1 Raoui, Y., Ez-Zahraouy, H., Tahiri, N., El Bounagui, O., Ahmad, S., Kazim, S., 2019.  
2 Performance analysis of MAPbI<sub>3</sub> based perovskite solar cells employing diverse charge selective  
3 contacts: Simulation study. Solar Energy 193, 948-955.
- 4 Saikia, D., Bera, J., Betal, A., Sahu, S., 2022. Performance evaluation of an all inorganic CsGeI<sub>3</sub>  
5 based perovskite solar cell by numerical simulation. Optical Materials 123, 111839.
- 6 Samiul Islam, M., Sobayel, K., Al-Kahtani, A., Islam, M., Muhammad, G., Amin, N.,  
7 Shahiduzzaman, M., Akhtaruzzaman, M., 2021. Defect study and modelling of SnX<sub>3</sub>-based  
8 perovskite solar cells with SCAPS-1D. Nanomaterials 11(5), 1218.
- 9 Slami, A., Bouchaour, M., Merad, L., 2020. Comparative study of modelling of Perovskite solar  
10 cell with different HTM layers. Int. J. Mater 7, 2313-10555.
- 11 Yang, W.S., Park, B.-W., Jung, E.H., Jeon, N.J., Kim, Y.C., Lee, D.U., Shin, S.S., Seo, J., Kim,  
12 E.K., Noh, J.H., 2017. Iodide management in formamidinium-lead-halide-based perovskite  
13 layers for efficient solar cells. Science 356(6345), 1376-1379.

14